The Astrophysical Journal, 913:141 (19pp), 2021 June 1 https://doi.org/10.3847/1538-4357/abf6d7

The GADOT Galaxy Survey: Dense Gas and Feedback in Herschel-selected Starburst Galaxies at Redshifts 2 to 6

Dominik A. Riechers[1], Asantha Cooray[2], Ismael Pérez-Fournon[3,4], and Roberto Neri[5]
[1] Cornell University, Space Sciences Building, Ithaca, NY 14853, USA; riechers@cornell.edu
[2] Department of Physics and Astronomy, University of California, Irvine, CA 92697, USA
[3] Instituto de Astrofisica de Canarias, E-38200 La Laguna, Tenerife, Spain
[4] Departamento de Astrofisica, Universidad de La Laguna, E-38205 La Laguna, Tenerife, Spain
[5] Institut de RadioAstronomie Millimétrique, 300 Rue de la Piscine, Domaine Universitaire, F-38406 Saint Martin d'Héres, France
Received 2021 January 25; revised 2021 March 28; accepted 2021 April 10; published 2021 June 4

Abstract

We report the detection of 23 OH^+ $1 \rightarrow 0$ absorption, emission, or P-Cygni-shaped lines and CO($J = 9 \rightarrow 8$) emission lines in 18 Herschel-selected $z = 2$–6 starburst galaxies with the Atacama Large Millimeter/submillimeter Array and the NOrthern Extended Millimeter Array, taken as part of the Gas And Dust Over cosmic Time Galaxy Survey. We find that the CO($J = 9 \rightarrow 8$) luminosity is higher than expected based on the far-infrared luminosity when compared to nearby star-forming galaxies. Together with the strength of the OH^+ emission components, this may suggest that shock excitation of warm, dense molecular gas is more prevalent in distant massive dusty starbursts than in nearby star-forming galaxies on average, perhaps due to an impact of galactic winds on the gas. OH^+ absorption is found to be ubiquitous in massive high-redshift starbursts, and is detected toward 89% of the sample. The majority of the sample shows evidence for outflows or inflows based on the velocity shifts of the OH^+ absorption/emission, with a comparable occurrence rate of both at the resolution of our observations. A small subsample appears to show outflow velocities in excess of their escape velocities. Thus, starburst-driven feedback appears to be important in the evolution of massive galaxies in their most active phases. We find a correlation between the OH^+ absorption optical depth and the dust temperature, which may suggest that warmer starbursts are more compact and have higher cosmic-ray energy densities, leading to more efficient OH^+ ion production. This is in agreement with a picture in which these high-redshift galaxies are "scaled-up" versions of the most intense nearby starbursts.

Unified Astronomy Thesaurus concepts: Active galaxies (17); Galaxy evolution (594); Starburst galaxies (1570); High-redshift galaxies (734); Infrared excess galaxies (789); Interstellar line emission (844); Interstellar line absorption (843); Submillimeter astronomy (1647); Millimeter astronomy (1061)

1. Introduction

The physical properties and chemical composition of the interstellar medium (ISM) set the initial conditions for star formation in galaxies through cosmic history. Following the initial detections of molecular gas at high redshift ($z > 1$) three decades ago (Brown & Vanden Bout 1991; Solomon et al. 1992), most studies in the early universe to date have focused on low- to mid-level CO rotational transitions, or the [CII] fine structure line (see Carilli & Walter 2013 for a review). These studies have recently resulted in the first measurements of the "cold gas history of the universe", i.e., the comoving volume density of molecular gas over ~13 billion years of cosmic time (e.g., Walter et al. 2014, 2020; Riechers et al. 2019, 2020a; Decarli et al. 2020; see also Klitsch et al. 2019; Lenkić et al. 2020). Molecular ions were first detected at high redshift 15 years ago through HCO^+, a tracer of the dense gas phase (García-Burillo et al. 2006; Riechers et al. 2006, 2010). Thanks to the emergence of sensitive submillimeter telescopes such as the Atacama Pathfinder Experiment (APEX), the Herschel Space Observatory, and more recently, the Atacama Large Millimeter/submillimeter Array (ALMA), studies of the ISM in the nearby universe have undergone a revolution, leading to the discovery of many missing links in the formation mechanisms of some of the key species, such as OH^+.

The reactive molecular ion OH^+ is a sensitive probe of the gas-phase oxygen chemistry in the ISM and the heating and excitation mechanisms associated with star formation and active galactic nuclei (AGNs). In particular, OH^+ reacts quickly with H_2 when present (or with free electrons through dissociative recombination), such that high ionization rates are required to retain a substantial abundance in the molecular phase of the ISM. Since the first interstellar detection of submillimeter-wave OH^+ absorption toward Sagittarius B2 (Wyrowski et al. 2010), it has been found that the absorbing gas appears to reside primarily in the atomic (HI) gas phase (e.g., Gerin et al. 2010; Neufeld et al. 2010). This conclusion is supported by the observed OH^+/H_2O^+ ratios, which indicate a comparatively low gas density (e.g., Benz et al. 2010). OH^+ in diffuse gas is formed primarily through ionization by cosmic rays, and thus is used to infer the cosmic-ray ionization rate in atomic hydrogen gas (e.g., Hollenbach et al. 2012; Indriolo et al. 2015, and references therein).

Outside the Milky Way, OH^+ absorption has been detected in nearby starbursts such as Arp 220 and M82 (Rangwala et al. 2011; Kamenetzky et al. 2012; González-Alfonso et al. 2013). More recently, these studies could be extended to the distant universe through the detection of OH^+ absorption or P-Cygni profiles in five starburst galaxies at $z = 2.3$–6.3 (Riechers et al. 2013, 2021; Indriolo et al. 2018; Berta et al. 2021). Based on the kinematic information from the line profiles referenced to the systemic redshifts (typically measured from CO emission lines), the absorption components in these intense starbursts

have been found to be associated with large-scale outflows or inflows, providing direct evidence for galaxy-scale feedback. OH^+ has also been detected purely in emission in the Orion Bar (van der Tak et al. 2013), as well as in nearby AGN host galaxies such as Mrk 231 and NGC 1068 (van der Werf et al. 2010; Spinoglio et al. 2012). OH^+ emission has recently even been detected in two AGN host galaxies at $z = 3$–6 (Li et al. 2020; Stanley et al. 2021).

In addition to newly discovered species, the study of high-J CO transitions has also been transformed by Herschel through the widespread detection of nearly complete CO line ladders up to CO($J = 13\rightarrow12$) and beyond in large samples of nearby galaxies (e.g., Kamenetzky et al. 2014; Rosenberg et al. 2015). These investigations have lead to a significantly more comprehensive understanding of the different heating and cooling mechanisms in the ISM of star-forming galaxies, and of the role of AGN versus ultraviolet and mechanical heating for the excitation of the CO line ladders. Building upon some of the initial high-redshift detections of high-J CO lines (beyond $J = 7\rightarrow6$) in AGN host galaxies (e.g., Downes et al. 1999; Weißet al. 2007; Bradford et al. 2009), the advent of ALMA and the upgraded NOrthern Extended Millimeter Array (NOEMA) have now made it possible to more routinely extend the studies of broadly sampled CO line ladders to dusty starburst galaxies (DSFGs), i.e., the most active, luminous massive star-forming galaxies to exist since the onset of galaxy formation (see, e.g., Hodge & da Cunha 2020 for a recent review).

A key aspect that has only been facilitated by a few studies to date is that telescopes such as ALMA and NOEMA offer sufficiently broad bandwidth toward studies of high-redshift galaxies to allow simultaneous coverage of high-J CO lines and other key species, including OH^+. Most relevant for this work, it is possible to simultaneously observe the CO($J = 9\rightarrow8$) and OH^+ $1_1\rightarrow0_1$ and $1_2\rightarrow0_1$ lines at rest frame $\sim$1 THz over a broad range in redshift. Because CO($J = 9\rightarrow8$) is most likely primarily associated with the warm, dense gas in the star-forming regions, it is a good indicator of the systemic redshift. Thus, the kinematic information entailed in the OH^+ lines can be referenced "in-band" to the systemic value from CO with minimum calibration biases.

We here report the detection of 20 ground-state OH^+ lines and 16 CO($J = 9\rightarrow8$) lines toward a sample of bright Herschel-selected DSFGs at $z = 2.3$–5.3 observed with ALMA and NOEMA. We also include observations of three OH^+ lines and two CO($J = 9\rightarrow8$) lines in two Herschel-selected targets from the literature (ADFS-27 at $z = 5.66$ and HFLS3 at $z = 6.34$; Riechers et al. 2013, 2021), which were obtained as part of our broader follow-up efforts of the parent sample from the Gas And Dust Over cosmic Time (GADOT) Galaxy Survey (D. Riechers et al. 2021, in preparation). We study relations between these diagnostic lines and the physical properties of the ISM and star-forming regions in distant galaxies in the context of our current understanding of high-mass galaxy formation. We present the data and their calibration in Section 2, before discussing the immediate results and presenting a broader analysis, informed by models and scaling relations, in Sections 3 and 4. A summary and conclusions are given in Section 5. We use a concordance, flat ΛCDM cosmology throughout, with $H_0 = 69.6$ km s^{-1} Mpc^{-1}, $\Omega_M = 0.286$, and $\Omega_\Lambda = 0.714$.

2. Data

2.1. Sample Properties

The full GADOT Galaxy Survey master sample is composed of $\sim$100 bright, Herschel-selected galaxies from the HerMES +HeLMS+HeRS and H-ATLAS surveys (Eales et al. 2010; Oliver et al. 2012) with spectroscopic redshifts. The majority of observations, including those presented here, focus on the subsample from the former survey, which itself consists of the "RARE" (i.e., the 500 μm brightest sources in the survey area; e.g., Conley et al. 2011; Riechers et al. 2011; Wardlow et al. 2013; Bussmann et al. 2015; Nayyeri et al. 2016; Gómez-Guijarro et al. 2019) and "red" (i.e., sources with $S_{250} < S_{350} < S_{500}$; e.g., Riechers et al. 2013; Dowell et al. 2014; Asboth et al. 2016) subsamples. The red subsample includes both strongly lensed sources that overlap with the RARE sample at the higher fluxes, and unlensed (or at most weakly lensed) hyperluminous infrared galaxies (HyLIRGs, or "Titans"; Riechers et al. 2017, 2021).

For our ALMA Atacama Compact Array/Morita Array (ACA) follow-up campaign, we selected 19 of the 250–500 μm brightest sources with spectroscopic redshifts in equatorial fields, with the goal of understanding their detailed ISM properties.[6] Three of these sources overlap with the red source catalog,[7] and three more sources are consistent with being red within the 1σ uncertainties of the 250–500 μm measurements.[8] From this sample of 19 sources, we here selected 13 sources for which the CO($J = 9\rightarrow8$) and OH^+($1_1\rightarrow0_1$) lines can be observed in a common tuning in bands 5–7, where observations in ACA standalone mode were offered by the observatory.[9]

Three additional sources were observed in the same lines as part of our NOEMA follow-up campaign of strongly lensed red sources. These galaxies were selected for an in-depth follow-up campaign because they make up all of the currently known strongly lensed $z > 5$ starbursts in the HerMES fields. As such, they are a natural extension of the ACA sample toward higher redshifts.

Spectroscopic redshifts for the full sample were obtained as part of our broader follow-up campaign (see Table 1 for details). With the exception of the weakly lensed merger HXMM-01, all sources in this sample are strongly gravitationally lensed, as revealed by ALMA, VLA, and Submillimeter Array (SMA) observations at 0.″05–0.″4 spatial resolution (Bussmann et al. 2015; Amvrosiadis et al. 2018; Geach et al. 2018; D. Riechers et al. 2021, in preparation). Together with observations of this new sample of 16 sources, we include previous CO($J = 9\rightarrow8$) and OH^+ detections in the $z = 5.66$ and 6.34 hyperluminous dusty starbursts ADFS-27 and HFLS3 that are also part of our master sample of $\sim$100 sources (Riechers et al. 2013, 2021). Neither of them is strongly lensed.

2.2. ALMA Observations

We observed the CO($J = 9\rightarrow8$) and OH^+($1_1\rightarrow0_1$) lines ($\nu_{rest} = 1036.9124$ and 1033.0582 GHz) toward 13 galaxies in our sample at $z = 2.29$–4.37 in bands 5–7 with the ALMA/

[6] Southern HerMES fields were not included due to a lack of spectroscopic redshifts at the time of the initial study.
[7] These sources are HeLMS-10, 28, and 65.
[8] These sources are Orochi and HeLMS-59 and 62.
[9] One additional source was observed in CO($J = 9\rightarrow8$), but the OH^+ line could not be covered by the tuning. We thus excluded the source from this work.

Table 1
ALMA/ACA and NOEMA Observations

Name[a]	HerMES/HeRS⋆ ID	Redshift	$\nu_{\rm obs}^{\rm CO(9-8)}$ (GHz)	Band	$N_{\rm ant}$	$\theta_{\rm maj}\times\theta_{\rm min}$ 290 μm	Observing Dates	$t_{\rm on}$ (min)	Complex Gain Calibrator	Bandpass/ Flux† Calib.
ALMA/ACA (6.4 hr):										
HeLMS-5 (HELMS8)	J004714.1+032453	2.2919[b]	314.9890	7	12	$4\farcs8 \times 3\farcs4$	2017 Sep 07	33.3	J0108+0135	J2253+1608 Uranus†
HeLMS-9 (HELMS18)	J005159.4+062240	2.3934[c]	305.5674	7	11	$5\farcs4 \times 3\farcs9$	2018 Nov 20	44.4	J0108+0135	J2258–2758
			169.8202[d]	5	11	$11\farcs2 \times 6\farcs3$[d]	2018 Dec 04	17.7	J0108+0135	J2258–2758
HeLMS-10 (HELMS10)	J005258.6+061317	4.3726[b]	193.0001	5	12	$10\farcs6 \times 5\farcs5$	2018 Nov 27	27.3	J0108+0135	J0237+2848
HeLMS-28 (HELMS4)	J004410.2+011821	4.1625[b]	200.8547	5	12	$7\farcs8 \times 5\farcs1$ $8\farcs2 \times 5\farcs4$[e]	2018 Nov 27	49.5	J0108+0135	J2253+1608
HeLMS-44 (HELMS2)	J233255.5–031134	2.6895[c]	281.0442	7	11	$6\farcs8 \times 3\farcs6$	2018 Oct 25	14.6	J2323–0317	J2253+1608
HeLMS-45 (HELMS7)	J232439.4–043934	2.4726[c]	298.5983	7	10	$7\farcs7 \times 3\farcs2$	2018 Oct 16	17.7	J2301–0158	J2258–2758
HeLMS-59 (HELMS6)	J233620.7–060826	3.4346[b]	233.8232	6	12	$8\farcs3 \times 4\farcs2$ $9\farcs0 \times 4\farcs5$[e]	2018 Oct 21	28.3	J2301–0158	J2258–2758
HeLMS-61 (HELMS15)	J233255.7–053424	2.4022[c]	304.7770	7	11	$5\farcs8 \times 3\farcs3$	2018 Oct 23	16.2	J2323–0317	J2253+1608
HeLMS-62 (HELMS5)	J234051.3–041937	3.5027[b]	230.2868	6	12	$8\farcs1 \times 4\farcs4$ $8\farcs5 \times 4\farcs7$[e]	2018 Oct 22	17.7	J0006–0623	J2258–2758
HeLMS-65 (HELMS_RED_31)	J002737.3–020759	3.7966[g]	216.1765	6	12	$9\farcs2 \times 4\farcs5$	2018 Oct 27	35.3	J2358–1020	J2253+1608
J0210+0016 (HeRS-1)	J020941.1+001557⋆	2.5534[f]	291.8085	7	12	$5\farcs3 \times 3\farcs5$	2018 Oct 21	15.1	J0217+0144	J0237+2848
HXMM-01 (XMM-01)	J022016.5–060143	2.3079[b]	313.4655	7	10	$5\farcs2 \times 3\farcs4$	2018 Oct 24	44.4	J0241–0815	J0423–0120
					12		2018 Oct 28			J0522–3627
Orochi (HXMM-02/XMM-06)	J021830.6–053131	3.3903[b]	236.1826	6	11	$6\farcs9 \times 4\farcs1$ $7\farcs3 \times 4\farcs4$[e]	2018 Nov 01	23.7	J0217–0820	J0423–0120
PdBI/NOEMA (14.2 hr):										
HeLMS-34 (HELMS_RED_4/ HELMS29)	J002220.9–015520	5.1614[g]	168.2917	2	5D	$5\farcs1 \times 3\farcs7$	2015 Sep 07	110	B0106+013	3C454.3 LkHA101†
HXMM-30 (XMM-30)	J022656.6–032709	5.094[g]	170.1530	2	6D	$4\farcs0 \times 2\farcs9$	2015 Sep 21	270	B0215+015	3C454.3 LkHA101† MWC 349†

Table 1
(Continued)

Name[a]	HerMES/HeRS* ID	Redshift	$\nu_{\rm obs}^{\rm CO(9-8)}$ (GHz)	Band	$N_{\rm ant}$	$\theta_{\rm maj}\times\theta_{\rm min}$ 290 μm	Observing Dates	$t_{\rm on}$ (min)	Complex Gain Calibrator	Bandpass/ Flux[†] Calib.
HLock-102 (Lock-102)	J104050.5+560652	5.2915[b]	164.8116	2	5D	$3\farcs9 \times 3\farcs5$	2013 Jun 12	470	B0954+556	3C84
							2013 Jul 04		B0954+556	3C279/3C454.3
							2013 Aug 17		B0954+658	LkHA101[†]
							2015 Sep 10		B0954+658	MWC 349[†]
GADOT literature sources:										
ADFS-27	J043657.7–543810	5.6550[g]	155.8095	4	46[h]	$0\farcs56 \times 0\farcs49$	2018 Nov 03	76	J0441–5154	J0519–4546
HFLS3	J170647.8+584623	6.3369[b]	141.3284	2	6S[i]	$4\farcs4 \times 3\farcs1$	2011 Dec 01/11	200	B1637+574	3C345/3C454.3
									B1849+670	MWC 349[†]

Notes.

[a] Alternative source names are from Wardlow et al. (2013), Asboth et al. (2016), or Nayyeri et al. (2016). Additional alternative source identifications are used throughout the literature; we here adopt those from the HerMES RARE source catalog, which allows for an easier identification of archival data.

[b] Redshift measured from 3 mm line scans with the Combined Array for Research in Millimeter-wave Astronomy (CARMA). The CARMA spectra of HeLMS-5 and HXMM-01 only showed single CO lines. The redshifts for these source were confirmed from 2 mm measurements with ALMA/ACA and NOEMA, respectively (D. Riechers et al., in preparation; see also Fu et al. 2013 for more details on HXMM-01). The redshift of HeLMS-5 reported here is updated from an incorrect value reported by Nayyeri et al. (2016), which was based on a single CO line and a submillimeter photometric redshift. Orochi was also discovered independently of the HerMES survey by Ikarashi et al. (2011).

[c] Redshift measured from 1 cm line scans with the Zpectrometer on the Green Bank Telescope (GBT), showing a single CO line per source, and confirmed with CARMA (A. Harris et al., in preparation; D. Riechers et al., in preparation).

[d] CO($J = 5\rightarrow4$) observations. Beam at 520 μm.

[e] Beam at 310 μm near the $OH^+(1_2\rightarrow0_1)$ line.

[f] Redshift determined at 1 cm and 3 mm with the GBT, CARMA, and the Large Millimeter Telescope (LMT; Geach et al. 2015; Harrington et al. 2016; Su et al. 2017).

[g] Redshift measured from 3 mm line scans with ALMA, and in the case of HeLMS-65, confirmed with the NSFs Karl G. Jansky Very Large Array (VLA; Riechers et al. 2017; D. Riechers et al., in preparation; see also Asboth et al. 2016).

[h] Observed with the ALMA 12 m array in the C43-5 configuration, covering 15 m–1.4 km baselines.

[i] Observed with PdBI/NOEMA in a special configuration between C and D.

ACA, using 10–12 7 m antennas covering 8.9–48.9 m baselines (see Table 1). For 4 galaxies, the redshifts also allowed us to cover the $OH^+(1_2\rightarrow0_1)$ line (ν_{rest} = 971.8053 GHz) in the same setups. Observations were carried out in cycles 4 and 6 under good to excellent weather conditions on 2017 September 07 and between 2018 October 16 and November 27 (project IDs: 2016.2.00105.S and 2018.1.00922.S; PI: Riechers), spending between 15 and 50 min on source for different targets depending on their expected line strengths. We also report CO($J=5\rightarrow4$) observations ($\nu_{rest}=576.2679$ GHz) for one target, carried out for 18 min on 2018 December 04 as part of the second program. Nearby radio quasars were observed for complex gain, bandpass, and absolute flux calibration, except for the two 2017 observing runs, which used Uranus as a flux calibrator (see Table 1; the bandpass and flux calibrators were identical where not listed separately). The absolute flux calibration is estimated to be reliable to within <10%.

The correlator was set up with two spectral windows of 1.875 GHz bandwidth (dual polarization) each per sideband, at a sideband separation of 8 GHz for all band 5 and 7 observations and typically 10 GHz for all band 6 observations (with some limited modifications to cover additional spectral lines in some cases). A spectral resolution of 31.25 MHz at a channel spacing of 15.625 MHz was chosen for all observations to reduce calibration overheads. Thus, neighboring channels in spectra shown at full resolution are not independent. In the current analysis, we only include contiguous spectral windows that contain OH^+ lines, and we defer the remaining part of the data to a future publication on other molecular species.

Data reduction was performed using version 5.4.0 or 5.6.1 of the CASA package (McMullin et al. 2007), aided by the calibration pipeline included with each version. Data were mapped manually using the CLEAN algorithm via the `tclean` task with "natural" baseline weighting, resulting in the synthesized beam sizes listed in Table 1. The main modification to the default pipeline was to reduce the edge channel flagging in some cases where they contained critical information, while still excluding channels with poor calibration. The rms noise values for the line and continuum emission in each data set are provided in the captions of Figures 1–5, and continuum-subtracted spectra are provided in Figures 6–9.

2.3. NOEMA Observations

We observed the CO($J=9\rightarrow8$) and $OH^+(1_1\rightarrow0_1)$ lines toward three galaxies in our sample at $z=5.09$–5.29 in band 2 with NOEMA. Observations were carried out with 5 or 6 antennas in the most compact D configuration under good weather conditions between 2013 June 12 and August 17 and between 2015 September 7 and 21 (project IDs: X045 and S15CY; PI: Riechers), spending between 110 and 470 min on source. Nearby radio quasars were observed for complex gain, bandpass, and absolute flux calibration (see Table 1), resulting in a flux scale that is reliable to within <10%. All observations were carried out with the WideX correlator, providing 3.6 GHz bandwidth (dual polarization) at 2 MHz spectral resolution.

Data reduction was performed using the GILDAS package. Data were mapped using the CLEAN algorithm with "natural" baseline weighting, resulting in the synthesized beam sizes listed in Table 1. The rms noise values for the line and continuum emission in each data set are provided in the captions of Figures 1 and 3, and continuum-subtracted spectra are provided in Figures 6 and 7.

3. Results

3.1. Continuum Emission

We successfully detect rest-frame 290 μm continuum emission at high peak signal-to-noise ratios (S/Ns) of 16–98 toward all 16 galaxies in the sample (Figure 1). We also detect rest-frame 310 μm emission in all 4 galaxies studied at this wavelength (Figure 4). We further detect rest-frame 520 μm emission toward HeLMS-9 as part of the CO($J=5\rightarrow4$) observations reported here (Figure 5). The dust continuum emission is only marginally resolved at most in all sources except for the large Einstein radius lenses HeLMS-9 and J0210 +0016, and only the former is fully resolved into two components corresponding to its lensing arcs (Figure 2). Continuum fluxes were extracted from two-dimensional Gaussian fitting in the image plane for all sources observed with ALMA, and from two-dimensional Gaussian fitting in the visibility plane for the sources observed with NOEMA (given the near-equatorial decl. and resulting limited uv coverage for two of the sources). Two Gaussian components were used for HeLMS-9, and the flux of both components was added by propagating the errors of each component. All continuum fluxes and uncertainties from the fitting are reported in Table 2. Given the high S/Ns of all detections, uncertainties are typically dominated by the absolute flux calibration, which is accounted for in our subsequent analysis. Comparison fluxes at standard wavelengths are provided in Table 4.

3.2. Line Emission and Absorption

3.2.1. CO Emission

We successfully detect CO($J=9\rightarrow8$) emission toward all 16 galaxies in the sample at peak S/Ns of 5–16 in the continuum-subtracted moment-0 maps (except for HeLMS-65, which is detected at a peak S/N of 4.2; Figure 1). The continuum subtraction was carried out in the visibility plane, and accounts for the spectral slope of the continuum where measurable within the line-free spectral ranges. The line emission is only marginally resolved at best in all cases except for HeLMS-9, which is resolved into two components. Line spectra were extracted centered on the peak positions of the line-averaged emission (Figure 6).

Line parameters were obtained from Gaussian fitting to the CO line profiles, using two Gaussian components where appropriate. Other lines in the bandpass were fitted simultaneously with additional Gaussian functions to include reliable estimates of the uncertainties of all fitting parameters, and the integrated line fluxes were compared to those found from two-dimensional Gaussian fitting to the emission in the moment-0 maps to warrant internal consistency. The resulting line fluxes are reported in Table 2, and the line luminosities are given in Table 4.

3.2.2. OH^+ Emission and Absorption

We successfully detect $OH^+(1_1\rightarrow0_1)$ emission or absorption toward all 16 galaxies in the sample, and $OH^+(1_2\rightarrow0_1)$ toward all 4 galaxies in which the line was covered (Figures 3 and 4). OH^+ absorption (emission) is detected or tentatively detected in 14/16 (10/16) sources. 2/16 sources show OH^+ emission,

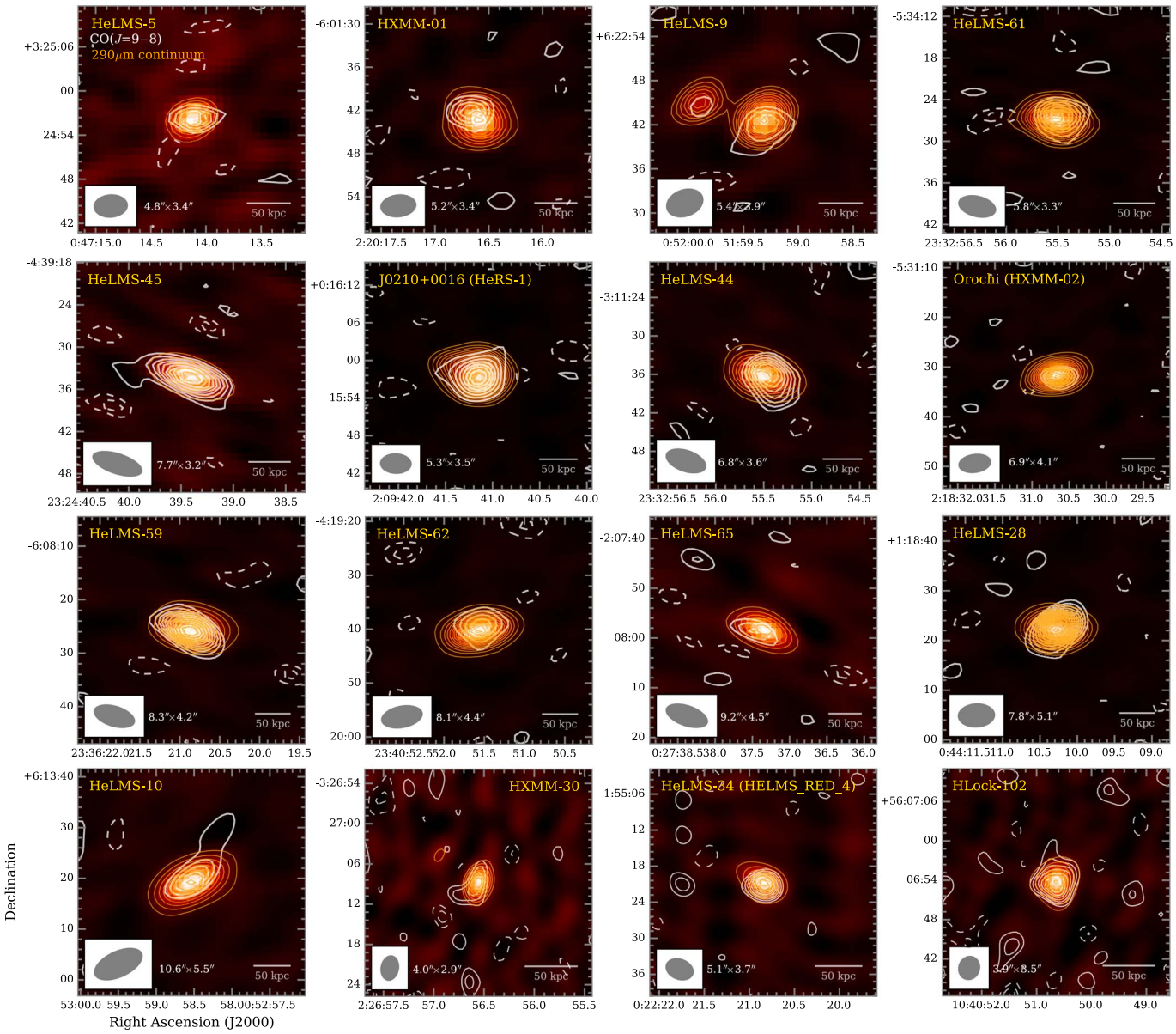

Figure 1. Rest-frame 290 μm dust continuum maps and contours (orange), overlaid with CO($J = 9\rightarrow8$) moment-0 contours (white) for the full sample, ordered with increasing redshift (the last three panels are NOEMA observations, the remainder are from ALMA/ACA). CO and dust emission is significantly detected in all sources and is cospatial to within the positional uncertainties (except for HXMM-01, where the CO emission may be dominated by the northern merger component). Dust continuum contours start at $\pm4\sigma$, and are shown in steps of $\pm4\sigma$, where $1\sigma = 1.28$, 0.42, 0.52, 0.39, 0.80, 0.90, 0.68, 0.33, 0.42, 0.45, 0.32, 0.26, 0.56, 0.27, 0.29, and 0.26 mJy beam^{-1}, respectively, except for HeLMS-5 and 9 and XMM-30, where contour steps are $\pm2\sigma$. CO contours start at $\pm2\sigma$ and are shown in steps of $\pm1\sigma = 1.33$, 1.08, 0.67, 0.39, 1.36, 0.84, 0.95, 0.56, 0.59, 1.87, 0.42, 0.57, 0.80, 0.41, 0.52, and 0.67 Jy km s^{-1}, respectively, except for J0210+0016, where contour steps are $\pm2\sigma$. The synthesized beam of the dust continuum map is shown in the bottom left corner of each panel, and the size is given.

but no absorption. 6/16 sources show OH^+ absorption, but no emission. 8/16 sources show evidence for both absorption and emission components when tentative detections are included. Three of the absorption lines are tentatively detected at peak S/Ns of 2.4–2.9, two are detected at moderate peak S/Ns of 3.3, and the remaining 12 lines are detected solidly at peak S/Ns of 4.6–11 (all S/Ns were estimated based on the continuum-subtracted moment-0 maps). The peak postions of the absorption features are always coincident with the continuum peak positions within the relative uncertainties. One of the emission lines is tentatively detected at a peak S/N of 2.5, five are detected at moderate peak S/Ns of 3.2–3.7, and seven are detected solidly at peak S/Ns of 4.1–9.1 (two sources, HeLMS-9 and 45, show multiple emission components). All detections are plausible, but independent confirmation is required for all features with S/N < 4 (S/N < 5 for sources that show potential spatial offsets from the CO and continuum peaks).

Line spectra were extracted centered on the peak positions of the line-averaged emission (Figures 7 and 8). Separate spectra were extracted for absorption and emission peaks where the positions may not coincide (HeLMS-44, 59, and 65, and HLock-102), and/or where multiple emission components are detected (HeLMS-9 and 45 only). Most of the offsets are marginal due to the moderate S/N of the emission components (see discussion in Section 3.3) and the potential interplay between emission/absorption components (such that OH^+ emission may be partially masked due to foreground OH^+

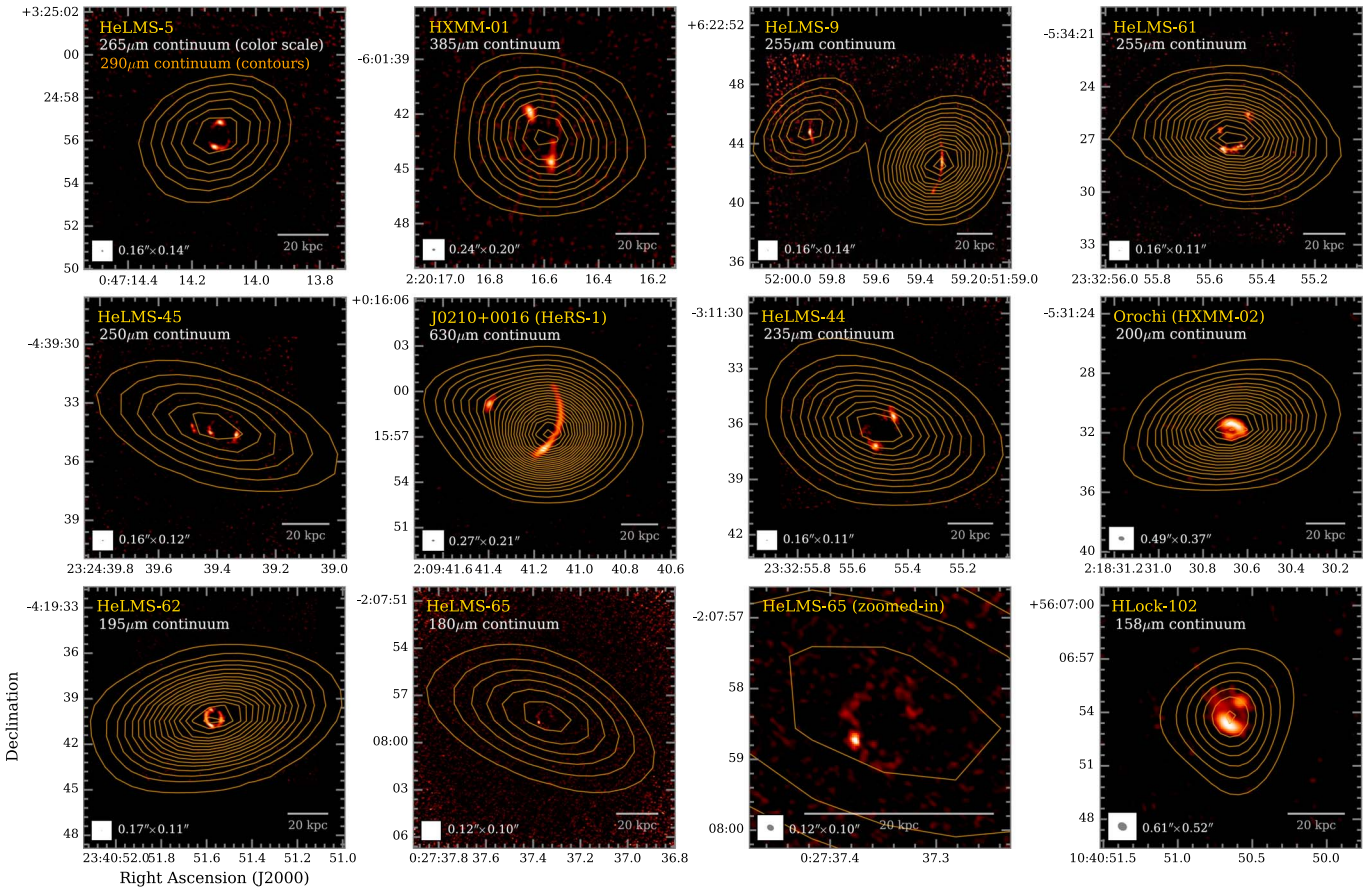

Figure 2. Same dust continuum contours as in Figure 1 (orange), but overlaid on ALMA (all except for HLock-102) or SMA dust continuum imaging at higher spatial resolution for 11 of the sources in our sample (color scale; data adopted from Bussmann et al. 2015; Oteo et al. 2017; Amvrosiadis et al. 2018; Geach et al. 2018; Xue et al. 2018; Greenslade et al. 2020; D. Riechers et al., in prep., but calibrated and imaged independently for most sources), based on availability in the literature. A second panel, zoomed-in by a factor of 4.5, is shown for HeLMS-65. The dust emission in the ALMA/ACA images is only substantially resolved for HeLMS-9 and J0210+0016, but strong lensing features are seen in all high-resolution images except for HXMM-01. The synthesized beam of the high-resolution images is shown in the bottom left corner of each panel, and the size is given. Increased noise toward the edges of some fields is due to the primary-beam correction.

absorption in some velocity ranges; see more detailed discussion below). As such, while our data may suggest that spatial offsets between absorption/emission components such as previously observed in ADFS-27 (Riechers et al. 2021) may not be uncommon, we defer a more general interpretation of absorption/emission peak position offsets to future work on higher-resolution data. Within the uncertainties, the $OH^+(1_1{\rightarrow}0_1)$ and $OH^+(1_2{\rightarrow}0_1)$ lines show the same profiles and velocities for all sources where both were covered, with the possible exception of HeLMS-62, where the absorption component of the former may be broader. The S/N of the $OH^+(1_2{\rightarrow}0_1)$ line in HeLMS-28 is too limited to warrant further interpretation, but it is possible that the red wing of the line is partially filled in by NH_2 emission, making the $OH^+(1_2{\rightarrow}0_1)$ line profile appear more asymmetric than the $OH^+(1_1{\rightarrow}0_1)$ line (see Section 3.3 for further discussion). Because of the limited width of the bandpass, the $OH^+(1_1{\rightarrow}0_1)$ features are only partially covered for HeLMS-59 and 62, but the $OH^+(1_2{\rightarrow}0_1)$ lines are virtually fully covered. As such, part of the interpretation of these sources is based on the latter lines alone.

Line parameters were obtained from Gaussian fitting to the OH^+ line profiles, using two Gaussian components where appropriate. The CO($J=9{\rightarrow}8$) lines (and other lines where appropriate) were fitted simultaneously with additional Gaussian functions to include reliable estimates of the uncertainties of all fitting parameters, and the integrated line fluxes were compared to those in the moment-0 maps to warrant internal consistency. The resulting line fluxes are reported in Table 2. HeLMS-9 shows a blueshifted OH^+ emission component that is sufficiently broad to be partially blended with the CO($J=9{\rightarrow}8$) line. To reliably separate both lines, we thus compared the CO($J=9{\rightarrow}8$) line profile to the CO($J=5{\rightarrow}4$) line profile (Figure 9), which shows a line width that is consistent with our multicomponent fits to the CO($J=9{\rightarrow}8$) and OH^+ features. The complexity of the OH^+ emission in this source (both spatially and spectrally) warrants further follow-up observations for a more detailed component separation.

Velocity shifts between the CO($J=9{\rightarrow}8$) (representing the systemic redshift) and OH^+ absorption and emission lines from the Gaussian fitting are provided in Table 3. All shifts were calculated at the centroid positions of each line. Values in parentheses are consistent with no shifts at the current S/N of our data. Nine sources show no significant velocity shifts in the absorption lines, while four and three sources show significant red- and blueshifts of the OH^+ absorption, respectively. The absorption velocity shifts are in the range of ∼130–360 km s^{-1}, which is typically less than the CO($J=9{\rightarrow}8$) line widths. Two sources show no significant velocity shifts in the emission lines, three show significant blueshifts, and five show significant redshifts. One source, HeLMS-9, shows components that are both blue- and redshifted, where the latter

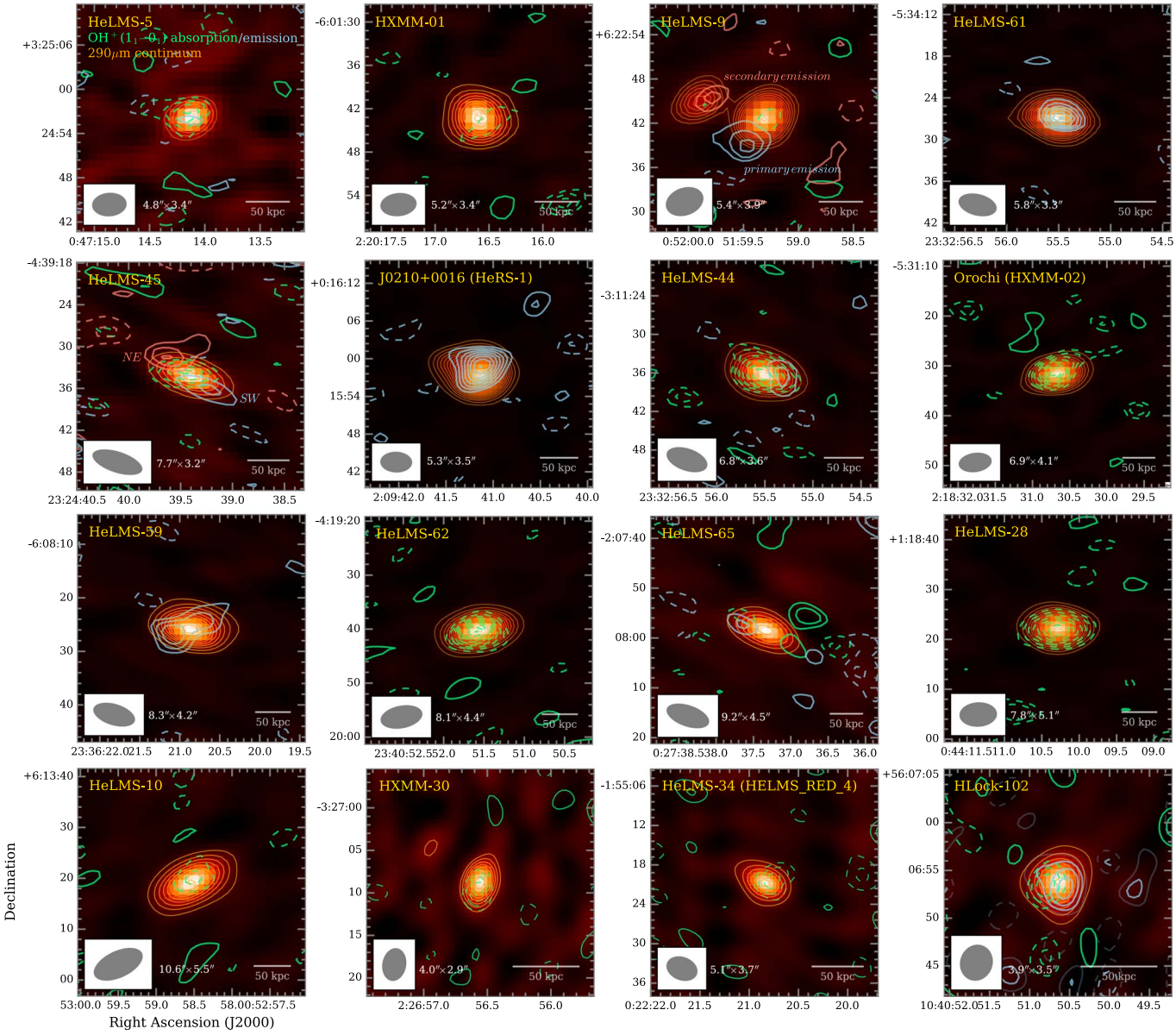

Figure 3. Same continuum emission as in Figure 1, but showing $OH^+(1_1 \rightarrow 0_1)$ instead of CO($J = 9 \rightarrow 8$). OH^+ absorption is displayed in dashed green contours, and OH^+ emission is displayed in blue contours where one component is detected, and in blue or red contours for bluer or redder components where multiple components are detected. OH^+ absorption contours are shown for all sources except for HeLMS-61, HeRS-1, and HeLMS-59, and start at $\pm 2\sigma$, progressing in steps of $\pm 1\sigma = 0.71$, 0.47, 0.26, 0.49, 0.63, 0.27, 0.49, 0.15, 0.27, 0.38, 0.57, 0.47, and 0.26 Jy km s^{-1}, respectively (the expected absorption component for HeLMS-59 fell outside the tuning range). OH^+ emission contours are shown for HeLMS-5, 9, 61, 45, J0210+0016, HeLMS-44, 59, 65, and HLock-102, and start at $\pm 2\sigma$, progressing in steps of $\pm 1\sigma = 0.58$, 0.30/0.63 (blue/red primary/secondary components), 0.37, 0.46/0.47 (blue/red southwest/northeast components), 0.82, 0.64, 0.35, 0.09, and 0.38 Jy km s^{-1}, respectively (the expected emission component for HeLMS-62 fell outside the tuning range). OH^+ absorption is detected or tentatively detected in 14/16 sources (see Figure 4 for HeLMS-59), and emission is detected or tentatively detected in 10/16 sources (see Figure 4 for HeLMS-62). Only 2/16 sources show OH^+ emission but no absorption.

component is closer to the CO($J = 9 \rightarrow 8$) and OH^+ absorption peaks. The emission velocity shifts are in the range of $\sim$30–1000 km s^{-1}. The highest redshifts exceed the CO($J = 9 \rightarrow 8$) line widths.

Blueshifted absorption and redshifted emission components (i.e., P-Cygni profiles) are expected for gas that is outflowing along the line of sight, while the opposite (i.e., inverse P-Cygni profiles) is expected for inflows. As such, the highest velocity emission components may be associated with outflowing gas beyond the escape velocities of their host galaxies. We caution that the centroid velocities alone may not always be sufficient to distinguish between inflows and outflows. As an example, the OH^+ emission centroid of HeLMS-59 appears to be significantly redshifted relative to CO from the spectral line fit alone (which would suggest an outflow), but it shows an inverse P-Cygni profile, and the strongest part of the emission is seen at blueshifted velocities. Thus, HeLMS-59 is most likely dominated by infalling material, even though we cannot rule out the presence of some outflowing gas. Overall, our sample appears to show similar numbers of examples of outflows and inflows based on velocity shifts alone under the assumption of simple spherical geometries, and a 3:2 ratio[10] when combining line profiles and velocity shifts, but

[10] This ratio would increase to 5:2 if we were to exclude the least significant identifications marked with a questionmark in Table 3.

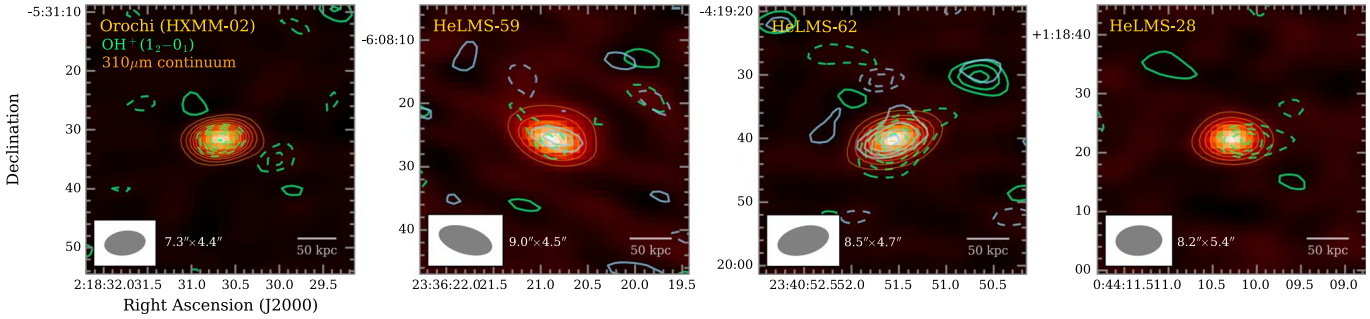

Figure 4. Same as Figure 3, but showing 310 μm dust continuum (color scale and orange contours) and OH$^+$(1_2→0_1) for the sources where the latter line was covered. Dust continuum contours are shown in steps of $\pm 4\sigma$, where $1\sigma = 0.34$, 0.78, 0.58, and 0.52 mJy beam^{-1}, respectively (left to right). OH$^+$ absorption contours (green) start at $\pm 2\sigma$ and are shown in steps of $\pm 1\sigma = 0.36$, 0.38, 0.48, and 0.31 Jy km s^{-1}, respectively. OH$^+$ emission contours (blue) for HeLMS-59 and 62 start at $\pm 2\sigma$ and are shown in steps of $\pm 1\sigma = 0.58$ and 0.91 Jy km s^{-1}, respectively.

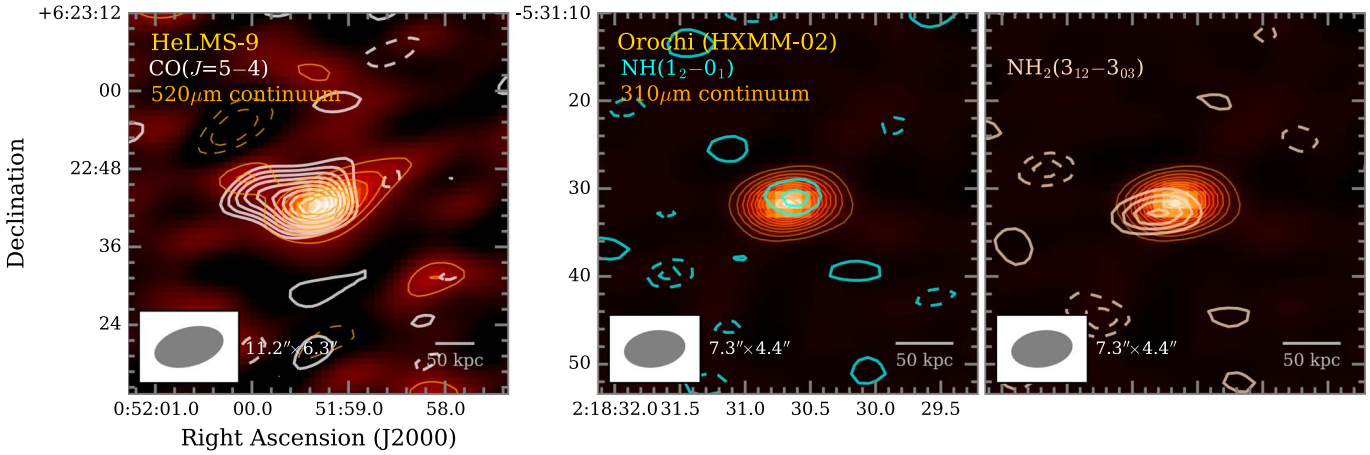

Figure 5. Rest-frame 520 μm dust continuum map and contours (orange), overlaid with CO($J = 5$→4) moment-0 contours (white) toward HeLMS-9 (left), and the same dust continuum contours as in Figure 4 for Orochi, overlaid with NH (middle; light blue) and NH_2 (right; light red) contours. Continuum contours for HeLMS-9 are shown in steps of $\pm 1\sigma = 0.32$ mJy beam^{-1}, starting at $\pm 2\sigma$. Line contours are shown in steps of $\pm 1\sigma = 0.93$, 0.40, and 0.44 Jy km s^{-1}, respectively (left to right), starting at $\pm 2\sigma$. The synthesized beam of the dust continuum map is shown in the bottom left corner of each panel, and the size is given.

observations at higher spatial resolution are desirable to study the gas kinematics and balance of outflows versus inflows on scales that come closer to resolving the starburst nuclei.

3.2.3. Other Lines

The OH$^+$(1_2→0_1) absorption feature in Orochi shows evidence for line emission both red- and blueward of the line (see the spectra extracted centered on the peak positions of the emission in Figure 8). Because no such emission is seen near the OH$^+$(1_1→0_1) absorption feature, these components are unlikely to be due to OH$^+$ emission, despite the fact that they appear to be symmetrically offset from the continuum peak position (Figure 5).[11]

We identify the blueward component at ~221.651–221.963 GHz (corresponding to –830 to –400 km s^{-1} relative to the systemic redshift of OH$^+$) detected at an S/N of ~3.5 with NH(1_2→0_1) line emission (which has 21 components at 974.3156 to 974.6078 GHz, with the strongest component at 974.4784 GHz, redshifted to 221.9246–221.9912 GHz and 221.9617 GHz, respectively). If correct, this would imply that the line centroid is redshifted by 185 ± 24 km s^{-1} relative to the systemic velocity, at a line full width at half maximum (FWHM) of 273 ± 61 km s^{-1} (i.e., comparable to that of the OH$^+$ absorption). Because this is significantly narrower than the CO($J = 9$→8) emission line, we cannot rule out that its red wing may be partially affected by absorption due to the (blueshifted) OH$^+$ line. This, however, is unlikely to be a strong effect due to the similarity in shape of both detected OH$^+$ absorption lines. We thus consider this identification to be plausible. We measure a line flux of 1.59 ± 0.45 Jy km s^{-1}, which corresponds to a line luminosity of $L'_{\rm NH(1-0)} = 1.1 \pm 0.3 \times 10^{10}$ K km s^{-1} pc^2.

We identify the redward component at ~220.853–221.228 GHz (corresponding to +170 to +680 km s^{-1} relative to the systemic redshift of OH$^+$) detected at an S/N of >5 with NH_2(3_{12}→3_{03}) line emission (which has seven of its components at 970.7079–970.7927 GHz, with the strongest component at 970.7883 GHz, redshifted to 221.1029–221.1222 GHz and 221.1212 GHz, respectively). If correct, the line centroid velocity of 17 ± 130 km s^{-1} would be consistent with the systemic redshift, and the line FWHM of 549 ± 225 km s^{-1} would be consistent with that of CO($J = 9$→8). The relatively large uncertainties on the line width are due to the proximity to the OH$^+$ absorption feature. We thus consider this identification to be plausible as well. We measure a line flux of 3.5 ± 1.2 Jy km s^{-1}, which corresponds to a line luminosity of $L'_{\rm NH2(312-303)} = 2.5 \pm 0.8 \times 10^{10}$ K km s^{-1} pc^2. Higher S/N measurements are desirable to more reliably deblend the different emission/absorption components, to investigate any red- or blueshifting of lines, and to more precisely constrain the

[11] We cannot rule out the presence of OH$^+$ emission components on smaller scales, however, that are diluted by the ACA beam with current data.

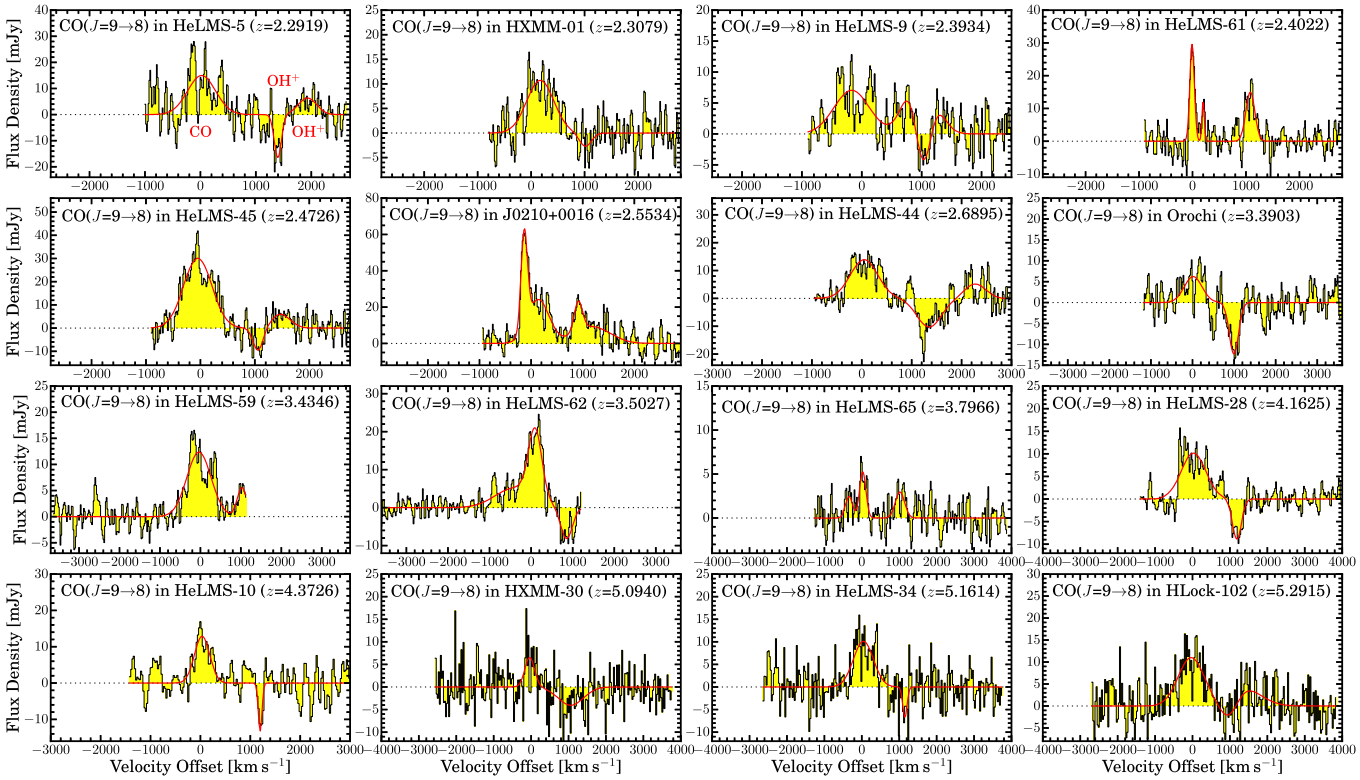

Figure 6. Spectra of CO($J = 9\rightarrow8$) emission lines (histograms) and Gaussian fits (red curves) to the line spectra, shown at 15.625 MHz spectral resolution. All spectra were extracted centered on the emission peaks in the moment-0 maps found after continuum subtraction (Figure 1). Significantly redward features are due to OH^+ absorption/emission (see Figure 7). All features were fitted simultaneously, but only the fit parameters for CO($J = 9\rightarrow8$) were adopted.

significance of any positional offsets for the NH and NH_2 detections at $z = 3.4$ in Orochi.

As discussed in the previous section, the $OH^+(1_2\rightarrow0_1)$ absorption feature in HeLMS-28 appears to be more asymmetric and potentially narrower than the $OH^+(1_1\rightarrow0_1)$ absorption feature. The shallower absorption is found at the velocities where $NH_2(3_{12}\rightarrow3_{03})$ emission would be expected. While the current S/N is too limited to attempt a reliable deblending, we thus consider it possible that NH_2 emission contributes to the apparent $OH^+(1_2\rightarrow0_1)$ profile. As a consequence, we base our further interpretation of this source mainly on the $OH^+(1_1\rightarrow0_1)$ line.

3.3. Position Offsets

Given the moderate spatial resolution of our observations, the main available spatial information are sizes and peak position offsets between different components. In all cases where the relevant information is available, the resolved sizes are consistent with what is expected from the Einstein radii or component separation at high spatial resolution (Figure 2), and the continuum peak positions are consistent with those seen in the dust emission at higher resolution. As such, we focus the remainder of our discussion on potential offsets from the dust continuum peaks.

The peaks of the CO($J = 9\rightarrow8$) emission coincide with those in the dust continuum within a fraction of the synthesized beam size, with one possible exception (Figure 1). In HXMM-01, the CO($J = 9\rightarrow8$) emission peaks to the northeast of the dust continuum peak. HXMM-01 is the only source in the sample that is thought to not be strongly lensed, but it consists of two galaxies of similar brightness (and a third, faint component) in the dust continuum (Figure 2; see also Fu et al. 2013; Bussmann et al. 2015). The peak of the CO($J = 9\rightarrow8$) emission appears to be consistent with the northern of the two galaxies. Our observations thus appear to suggest that this galaxy dominates the high-J line emission.

The peaks of all OH^+ absorption lines coincide with the dust continuum peaks in all cases, as expected. Minor offsets are only seen in the sources with the lowest S/Ns, and thus are not significant given the noise variations in the maps.

The OH^+ emission peaks are coincident with the dust continuum peaks in most cases, with a few possible exceptions. The emission in HeLMS-65 is too weak for the offset to be considered reliable. HeLMS-9 shows two emission components, one for each of the two lensed arcs. The redshifted component is superposed in velocity with the OH^+ absorption component, such that the apparent offset from the dust continuum peak may be due to the fact that the emission is reduced due to absorption in the foreground at that position. The blueshifted peak has a lower S/N, and it also is impacted by a mix of absorption and emission near the systemic redshift. HeLMS-45 (which appears to show two emission components) and 44 (which may show a tentative offset in a similar direction as CO) may also show spatial offsets, but in contrast to HeLMS-9, it remains unclear whether there is a significant velocity overlap between the absorption and emission components. Because the S/N of the emission components for both of these sources is only moderate, it cannot be ruled out with the current data that the spatial offsets are due to residual uncertainties in the deblending of different components. Higher-resolution imaging at better sensitivity is required to

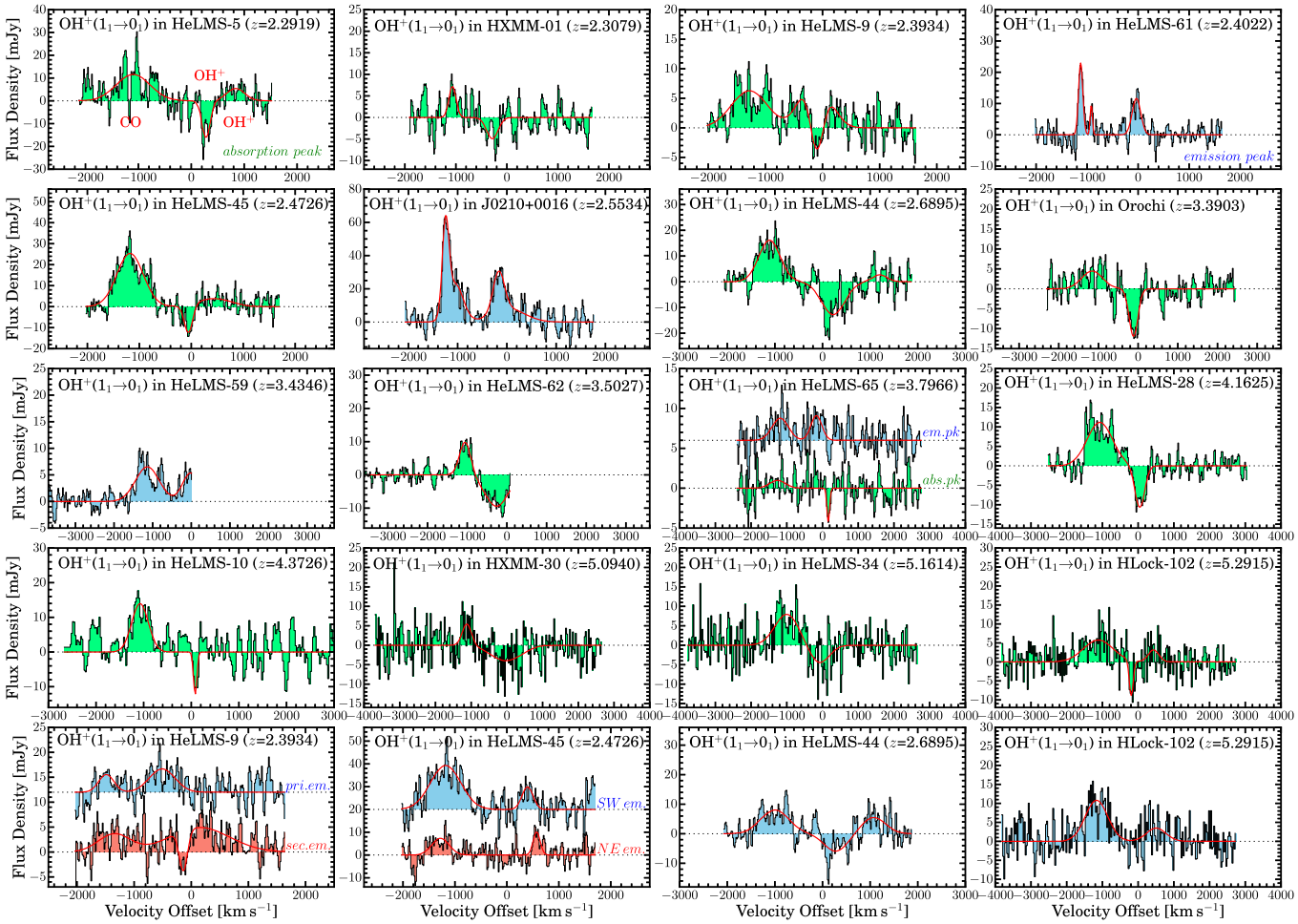

Figure 7. Spectra of $OH^+(1_1 \rightarrow 0_1)$ absorption/emission lines (histograms) and Gaussian fits (red curves) to the line spectra, shown at 15.625 MHz spectral resolution. All spectra were extracted centered on the absorption (green) or emission peaks (blue) in the moment-0 maps found after continuum subtraction (Figure 3). Red histograms are used for the redder emission components in sources that show multiple emission components (i.e., the component toward the fainter lensed image of HeLMS-9, and the northeastern (NE) emission component toward HeLMS-45). Secondary components are offset on the *y*-axis for clarity. The same color-coding is used as in the contour maps in Figure 3. All features were fitted simultaneously, but only the fit parameters for OH^+ were adopted.

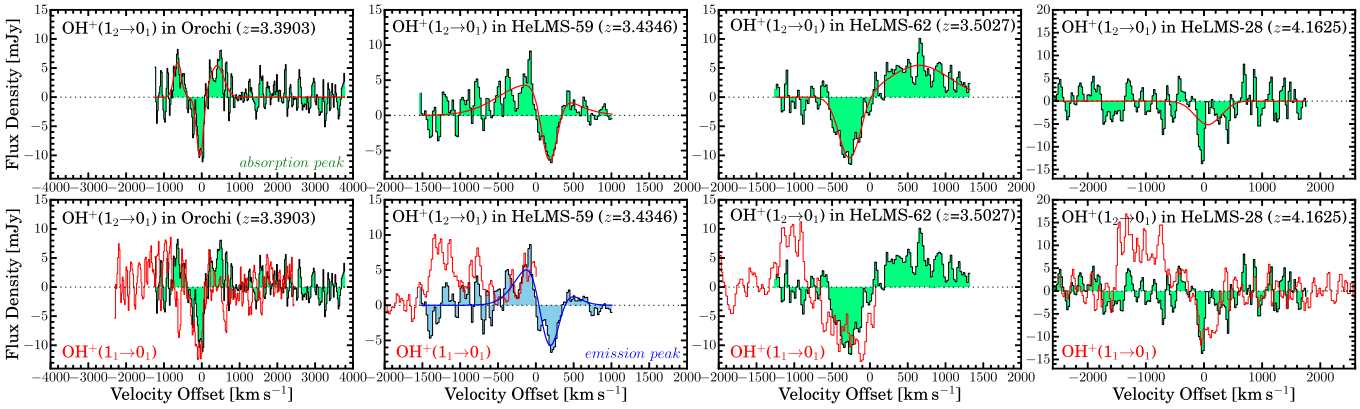

Figure 8. Spectra of $OH^+(1_2 \rightarrow 0_1)$ absorption/emission lines (histograms) and Gaussian fits (red curves) to the line spectra (top) and comparison to the $OH^+(1_1 \rightarrow 0_1)$ spectra (bottom), all shown at 15.625 MHz spectral resolution. All spectra were extracted centered on the absorption peaks in the moment-0 maps found after continuum subtraction (Figure 4), except for the bottom panel for HeLMS-59, which was extracted centered on the emission peak (where the blue curve shows a Gaussian fit to this spectrum). The same color-coding is used as in the contour maps in Figure 4. CO($J = 9 \rightarrow 8$) emission was not subtracted from the comparison spectra. Bottom left: The OH^+ $1_2 \rightarrow 0_1$ and $1_1 \rightarrow 0_1$ absorption features in Orochi show comparable line profiles, but the former spectrum shows additional emission at velocities where none is seen in the latter. The emission thus is unlikely to be due to OH^+ (see Figure 9 for line identifications). All features were fitted simultaneously, but only the fit parameters for OH^+ were adopted.

provide a more detailed interpretation for any of these sources. Comparing the emission components in the two OH^+ lines for HeLMS-59, the apparent finite extent seen in the $OH^+(1_1 \rightarrow 0_1)$ line may be due to the less reliable phase calibration at the outer edge of the bandpass, where the emission peaks. We thus do not consider it significant, and we focus on the (fully covered)

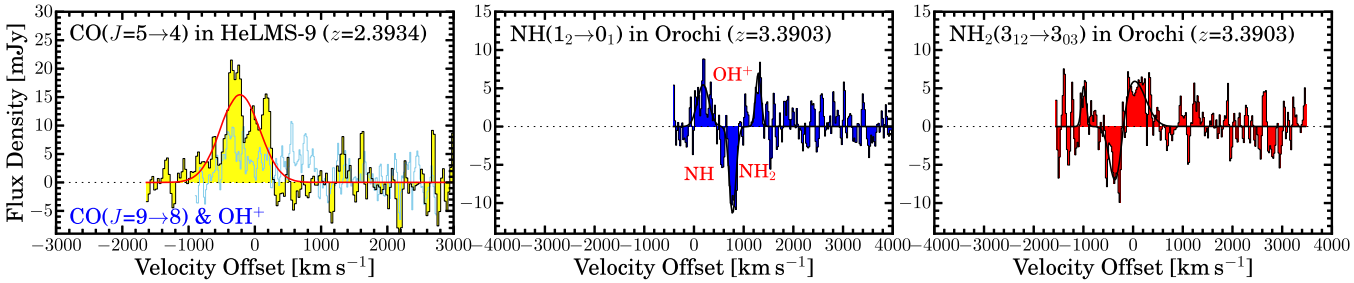

Figure 9. Spectra of emission lines other than CO($J = 9\rightarrow8$) or OH^+, shown at 15.625 MHz spectral resolution, and Gaussian fits (red curves) to the line spectra. All spectra were extracted centered on the emission peaks in the moment-0 maps found after continuum subtraction (Figure 5). Left: The overlay of the CO($J = 5\rightarrow4$) (yellow histogram) and CO($J = 9\rightarrow8$) (light blue) line spectra toward HeLMS-9 shows that the redward emission component observed in the latter is not seen in the former, and thus is most likely due to blueshifted OH^+ emission. This is consistent with the spectral decompositions shown in Figures 6 and 7, which assume that the emission at +400–1000 km s^{-1} is associated with OH^+, not CO. Middle and right: The emission components in the $OH^+(1_2\rightarrow0_1)$ spectrum are consistent with redshifted NH emission (middle) and NH_2 emission at the systemic velocity (right). All features were fitted simultaneously, but only the fit parameters for NH (middle) or NH_2 (right) were adopted.

$OH^+(1_2\rightarrow0_1)$ line for most of the interpretation in the following.

For J0210+0016, the OH^+ emission appears to peak closer to the center of the main lensed arc of the source than the dust continuum. This source is thought to contain an AGN (e.g., Geach et al. 2018), which may impact the OH^+ formation mechanisms in part of the galaxy. Because J0210+0016 shows no evidence for OH^+ absorption at the sensitivity limit of our data, we conclude that it is the only target for which the OH^+ emission peak offset can be considered significant at present.

4. Analysis and Discussion

4.1. Spectral Energy Distribution Modeling

To determine the dust properties of our sample, we fit modified blackbody models to the rest-frame far-infrared (FIR) to submillimeter wavelength emission using the Markov chain Monte Carlo based approach MBB_EMCEE described in more detail by Riechers et al. (2013) and Dowell et al. (2014). This method uses the dust temperature $T_{\rm dust}$, the spectral slope of the dust emissivity $\beta_{\rm IR}$, and the wavelength λ_0 where the optical depth reaches unity as the main fit parameters. To capture the approximate shape of the spectral energy distribution (SED) on the far Wien side, we join the MBB to a ν^{α} power law at short wavelengths. The observed-frame 500 μm flux density is used as a normalization parameter of the fits. To guide the fitting process, we place a broad prior of $\beta_{\rm IR} = 1.8 \pm 0.6$ on the emissivity parameter (i.e., centered on the value for Milky Way molecular clouds; e.g., Planck Collaboration et al. 2011), and leave all other parameters without a prior. The results for the entire sample are reported in Table 4 and shown in Figure 10, also including our previous fits for ADFS-27 and HFLS3 (Riechers et al. 2013, 2021). We also re-fit four comparison sources at $z = 2.3$–3.0 with either OH^+ or CO($J = 9\rightarrow8$) detections (including two sources where both lines were either solidly or tentatively detected) from the literature to enable a meaningful comparison, and have included the resulting values in Table 4.

For the GADOT sample, we find median values of $T_{\rm dust} = 56.9 \pm 3.1$ K, $\beta_{\rm IR} = 2.0 \pm 0.3$, and λ_0=201 $\pm$ 38 μm, where the quoted uncertainties are the median absolute deviation. The median peak wavelength of the SEDs is $\lambda_{\rm peak}$=86 $\pm$ 7 μm. The range in apparent S_{250} is a factor of $\sim$70 ($\sim$30 when only strongly lensed sources are included), while the range in apparent far-infrared luminosity $L_{\rm FIR}$ is only a factor of $\sim$8. Because the range in $T_{\rm dust}$ ($\lambda_{\rm peak}$) is only a factor of $\sim$1.7 (1.5), this difference is largely due to the large range in redshift spanned by the sample. This is consistent with the factor of $\sim$7 range in S_{870}, i.e., at a wavelength where the negative K-correction is much stronger than at 250 μm. The range in λ_0 is a factor of $\sim$2.9, but for all sources, λ_0 is smaller than the rest wavelengths of the OH^+ $1_1\rightarrow0_1$ and $1_2\rightarrow0_1$ lines. Thus, the dust is expected to only be moderately optically thick toward (or behind) the observed absorption/emission lines.

4.2. Scaling Relations

4.2.1. CO(J = 9→8)–FIR and OH^+–FIR Relations

We find a strong correlation between the CO($J = 9\rightarrow8$) line ($L'_{\rm CO(9-8)}$) and FIR dust continuum luminosities for the GADOT sample (Figure 11 left). This relation is reminiscent of that found for nearby star-forming galaxies (e.g., Liu et al. 2015), consistent with the idea that the CO($J = 9\rightarrow8$) emission is associated with warm, dense molecular gas in the star-forming regions. The GADOT sample is consistent with the linear slope of the relation found for the lower-luminosity nearby galaxies, but the sample appears to be systematically offset toward higher CO($J = 9\rightarrow8$) luminosity.

At first glance, one may conclude that this could be due to the fact that most GADOT sources are strongly lensed, given that no magnification correction has been applied. However, given the linear slope of the relation, such corrections would only be important if there is differential lensing between the $\sim$70–100 μm dust near the peak of the SEDs and the warm, dense molecular gas. Moreover, the observed offset is in the opposite direction of what would be expected for differential lensing between a compact, warm dust component and a more extended molecular gas component.

Another possibility would be that the gas excitation in the GADOT sample is systematically higher than in the nearby galaxies. To further investigate this issue, Figure 11 highlights the galaxies that overlap with the Class I, II, and III samples of the HerCULES survey (Rosenberg et al. 2015), where a higher class corresponds to a higher CO excitation. Indeed, Class I sources appear to show systematically lower CO($J = 9\rightarrow8$) to FIR luminosity ratios than the Class II and III samples, and Class II sources appear to preferentially fall within the intermediate range. This is consistent with the idea that differences in CO excitation may be responsible for a significant portion of the observed scatter of the relation. Class III sources show the broadest scatter, with about half of them

Table 2
Line and Continuum Parameters

Name	Redshift	$I_{CO(9-8)}$ (Jy km s^{-1})	$dv_{CO\ (9-8)}$ (km s^{-1})	$I^{abs}_{OH+(11-01)}$ (Jy km s^{-1})	$dv^{abs}_{OH+(11-01)}$ (km s^{-1})	$I^{em}_{OH+(11-01)}$ (Jy km s^{-1})	$dv^{em}_{OH+(11-01)}$ (km s^{-1})	$I^{abs}_{OH+(12-01)}$ (Jy km s^{-1})	$dv^{abs}_{OH+(12-01)}$ (km s^{-1})	$I^{em}_{OH+(12-01)}$ (Jy km s^{-1})	$dv^{em}_{OH+(12-01)}$ (km s^{-1})	S_{290} (mJy)	S_{310} (mJy)
HeLMS-5	2.2919	9.1 ± 1.4	596 ± 81	–3.36 ± 0.65	186 ± 34	*1.55 ± 0.62*	*386 ± 145*					25.4 ± 1.7	
HXMM-01	2.3079	7.3 ± 1.2	600 ± 55	*–1.38 ± 0.47*	*265 ± 72*							27.92 ± 0.97	
HeLMS-9[a]	2.3934	6.7 ± 1.3	694 ± 90	*–0.81 ± 0.29*	*292 ± 78*	3.7 ± 1.1(e)	1248 ± 235					29.6 ± 1.7	
						1.16 ± 0.33(w)	531 ± 90						
HeLMS-61	2.4022	3.81 ± 0.48	100 ± 8			2.89 ± 0.40	199 ± 23					32.89 ± 0.78	
			52 ± 14										
HeLMS-45	2.4726	18.9 ± 2.7	610 ± 31	–2.90 ± 0.55	191 ± 40	*2.01 ± 0.49(ne)*	*160 ± 35*					22.3 ± 1.2	
						1.98 ± 0.62(sw)	251 ± 62						
J0210+0016	2.5534	19.2 ± 1.7	146 ± 12			11.6 ± 1.8	272 ± 38					149.4 ± 6.2	
			490 ± 56				797 ± 210						
HeLMS-44	2.6895	11.5 ± 1.9	648 ± 72	–6.93 ± 0.88	573 ± 59	2.56 ± 0.76	591 ± 194					39.3 ± 1.1	
Orochi	3.3903	4.03 ± 0.61	505 ± 103	–2.84 ± 0.47	259 ± 31			–2.76 ± 0.39	215 ± 30			24.09 ± 0.54	17.72 ± 0.35
HeLMS-59	3.4346	8.9 ± 1.0	708 ± 44	*(not covered)*		>1.66 ± 0.33[c]	494 ± 205[c]	–1.40 ± 0.48	247 ± 29	2.30 ± 0.62	613 ± 97[e]	25.41 ± 0.95	21.2 ± 1.5
HeLMS-62	3.5027	11.8 ± 2.3	380 ± 47	–5.59 ± 0.50	683 ± 81	*(not covered)*		–4.77 ± 0.78	337 ± 28	5.2 ± 1.2	933 ± 120	32.15 ± 0.43	21.79 ± 0.90
			1114 ± 310										
HeLMS-65	3.7966	1.61 ± 0.38	201 ± 37	*–0.34 ± 0.14*	*89 ± 30*	1.66 ± 0.51	363 ± 92					8.66 ± 0.28	
			222 ± 83										
HeLMS-28	4.1625	8.36 ± 0.70	776 ± 59	–3.33 ± 0.37	324 ± 38			–1.69 ± 0.34	524 ± 125[d]			18.40 ± 0.24	14.66 ± 0.37
HeLMS-10	4.3726	4.72 ± 0.84	360 ± 52	–1.36 ± 0.42	85 ± 104							21.82 ± 0.99	
HXMM-30	5.094	2.18 ± 0.44	307 ± 101	–3.45 ± 0.61	999 ± 347							5.81 ± 0.45	
HeLMS-34	5.1614	5.82 ± 0.56	632 ± 90	–2.68 ± 0.58	643 ± 321							7.88 ± 0.55	
HLock-102	5.2915	9.7 ± 1.5	777 ± 99	–1.35 ± 0.27	132 ± 40	3.45 ± 0.64	645 ± 280					10.27 ± 0.66	
ADFS-27[b]	5.6550	1.80 ± 0.04	597 ± 18	–2.96 ± 0.027	422 ± 50	0.147 ± 0.018	745 ± 87	*(not covered)*		0.17 ± 0.04	∼740	2.67 ± 0.05	2.09 ± 0.05
HFLS3[b]	6.3369	2.77 ± 0.45	497 ± 107	–0.56 ± 0.18	416 ± 170	>0.90[c]	>765					3.22 ± 0.12	2.38 ± 0.11

Notes. Tentative detections are indicated in italic font.

[a] The CO($J = 5\rightarrow4$) FWHM line width is $dv_{CO(5-4)} = 700 \pm 64$ km s^{-1}. This shows that the broadened component is due to OH$^+$ emission, not CO($J = 9\rightarrow8$). The 520 μm continuum flux is $S_{520} = 3.69 \pm 0.48$ mJy.

[b] Adopted from Riechers et al. (2013, 2021).

[c] Component not fully covered by the bandpass.

[d] Fit to the line profile includes a moderate S/N component, and thus is less reliable than that to the OH$^+$($1_1\rightarrow0_1$) line.

[e] Line may include a broad wing, which if confirmed would increase the best estimate to 995 ± 171 km s^{-1}. If real, this would likely also imply some contribution of OH$^+$($1_1\rightarrow0_1$) emission to the measured CO($J = 9\rightarrow8$) line flux.

Table 3
Line Shifts and OH^+ Optical Depths

Name	Redshift	$v_0^{OH+,abs}-v_0^{CO}$ (km s^{-1})	$v_0^{OH+,em}-v_0^{CO}$ (km s^{-1})	Origin	τ_{OH+}	$\tau_{OH+}dv$ (km s^{-1})	$N(OH^+)$[a] (10^{14} cm^{-2})	$L'^{em}_{OH^+(1-0)}$[b] (10^{10} L_l)
HeLMS-5	2.2919	258 ± 33	*(795 ± 63)*	ambiguous	$1.3^{+0.7}_{-0.4}$	343^{+186}_{-109}	$16.7^{+9.0}_{-5.3}$	*0.50 ± 0.20*
HXMM-01	2.3079	*(–457 ± 36)*		ambiguous	$0.32^{+0.14}_{-0.12}$	116^{+50}_{-44}	$5.6^{+2.4}_{-2.1}$	
HeLMS-9	2.3934	*(68 ± 35)*	–341 ± 48(e) 313 ± 77(w)	ambiguous	$0.25^{+0.10}_{-0.11}$	53^{+23}_{-21}	$2.6^{+1.1}_{-1.0}$	1.69 ± 0.40
HeLMS-61	2.4022		–26 ± 10	inflow?				1.01 ± 0.14
HeLMS-45	2.4726	(–6 ± 17)	–232 ± 11 *(622 ± 18)(ne)* 397 ± 25(sw)	outflow	$0.55^{+0.15}_{-0.13}$	173^{+47}_{-41}	$8.4^{+2.3}_{-2.0}$	1.47 ± 0.29
J0210+0016	2.5534		–32 ± 15	inflow?				4.52 ± 0.70
HeLMS-44	2.6895	177 ± 36	1026 ± 61	outflow?	$0.30^{+0.05}_{-0.04}$	179^{+27}_{-26}	$8.7^{+1.3}_{-1.3}$	1.09 ± 0.32
Orochi	3.3903	–132 ± 41		outflow	0.43 ± 0.09	146^{+32}_{-29}	$7.1^{+1.5}_{-1.4}$	
HeLMS-59[c]	3.4346	213 ± 20	94 ± 60	inflow	$0.26^{+0.11}_{-0.10}$	88^{+36}_{-33}	$2.5^{+1.0}_{-0.9}$	1.66 ± 0.45
HeLMS-62[c]	3.5027	–363 ± 15	561 ± 37	outflow	$0.46^{+0.10}_{-0.09}$	199^{+43}_{-39}	$11.1^{+1.4}_{-1.3}$	3.88 ± 0.89
HeLMS-65	3.7966	*(136 ± 20)* *(502 ± 36)*	–197 ± 40	inflow	$1.88^{+\infty}_{-1.19}$	$244^{+\infty}_{-154}$	$11.9^{+\infty}_{-7.5}$	1.25 ± 0.38
HeLMS-28	4.1625	(20 ± 28)		ambiguous	$0.40^{+0.06}_{-0.05}$	161^{+23}_{-21}	$7.8^{+1.1}_{-1.0}$	
HeLMS-10	4.3726	(49 ± 49)		ambiguous	$0.57^{+0.27}_{-0.21}$	83^{+39}_{-31}	$4.0^{+1.9}_{-1.5}$	
HXMM-30	5.094	(16 ± 139)		ambiguous	$1.43^{+0.83}_{-0.45}$	1109^{+642}_{-346}	54^{+31}_{-17}	
HeLMS-34	5.1614	(–133 ± 150)		ambiguous	$0.75^{+0.27}_{-0.21}$	417^{+153}_{-120}	$20.3^{+7.5}_{-5.8}$	
HLock-102	5.2915	(–152 ± 159)	544 ± 193	outflow	$1.90^{+\infty}_{-0.76}$	$381^{+\infty}_{-152}$	$18.5^{+\infty}_{-7.4}$	4.33 ± 0.80
ADFS-27[d]	5.6550	–216 ± 16	233 ± 10	outflow	0.35 ± 0.04	234 ± 26	11.4 ± 1.2	0.20 ± 0.02
HFLS3[d]	6.3369	179 ± 74	…[e]	ambiguous	$0.49^{+0.21}_{-0.17}$	205^{+87}_{-72}	$10.0^{+4.2}_{-3.5}$	>1.48

Notes. Tentative detections are indicated in italic font. Values in parentheses are consistent with no velocity shifts (tentative detections are included in this category by default). "Origin" is the most likely interpretation based on the presence of P-Cygni (outflow) or inverse P-Cygni (inflow) profiles, or when not available or ambiguous, the blue- or redshift of the absorption and emission components.

[a] These values can be translated into approximate neutral H I column densities by assuming a relative abundance of $[OH^+/H] = -7.8$, i.e., by multiplying the listed values by a factor of 6.3×10^7 (e.g., Bialy et al. 2019).

[b] Given in units of L_l = K km s^{-1} pc^2. Apparent values not corrected for gravitational magnification where applicable.

[c] Velocity shifts and $L'^{em}_{OH^+(1-0)}$ are reported relative to OH^+ $1_2 \rightarrow 0_1$ instead of $1_1 \rightarrow 0_1$ due to the incomplete coverage of the latter by our observations.

[d] Adopted from Riechers et al. (2013, 2021).

[e] Component not fully covered by the bandpass.

being below the relation, in a similar region as the GADOT sources. The strongest outlier is the binary AGN NGC 6240, which shows the highest $L'_{CO(9-8)}/L_{FIR}$ ratio of the entire combined low- and high-redshift sample. The high CO line to dust continuum luminosity ratio in NGC 6240 is thought to be due to shock excitation (e.g., Meijerink et al. 2013). At face value, our findings may therefore suggest more prevalent shock excitation (rather than stronger radiative excitation due to the warm dust or hidden AGNs) in DSFGs at $z = 2$–6 than in most nearby star-forming galaxies, perhaps due to slow-moving shocks. A possible alternative explanation would be that these galaxies exhibit increased cosmic-ray energy densities that lead to an increased CO excitation.[12]

We also find a weak correlation between the OH^+ line emission components ($L'^{em}_{OH^+(1-0)}$) and FIR dust continuum luminosities for the GADOT sample (Figure 11 right), with a best fit of $\log(L_{FIR}/L_\odot) = (5.5 \pm 2.5) + (0.35 \pm 0.10)$ $\log(L'^{em}_{OH^+(1-0)}/L_l)$, where L_l=K km s^{-1} pc^2. The OH^+ emission components are consistent with being associated with shock-heated, dense gas components impacted by galactic winds (e.g., Falgarone et al. 2017; Riechers et al. 2021). As discussed above, the presence of shock-heated gas is consistent with the strong CO($J = 9 \rightarrow 8$) emission across the GADOT sample. Thus, while we cannot make strong inferences based on this relation alone, and while alternative scenarios cannot be ruled out, our findings for the CO and OH^+ emission paint a consistent picture for the heating and excitation mechanisms in $z = 2$–6 DSFGs.

4.2.2. OH^+ Opacity Relations

The OH^+ absorption components are likely associated with cool ($\lesssim$100 K), low-density (<100 cm^{-3}), spatially extended gas components along the line of sight to the warm dust continuum emission from the starbursts (e.g., Falgarone et al. 2017; Riechers et al. 2021).

To better understand the implications of the OH^+ absorption detections in our sample, we have calculated the peak optical depths $\tau_{OH+} = -\ln(f_{trans})$ and the velocity-integrated optical depths $\tau_{OH+}\,dv$ (which is a quantity similar to the line equivalent width) for the GADOT sample. Here, f_{trans} is the fraction of the continuum emission that is still transmitted. The resulting values are summarized in Table 3. The GADOT sample has a median $\tau_{OH+} = 0.56 \pm 0.25$ and a median $\tau_{OH+}\,dv = 220 \pm 110$ km s^{-1}. This corresponds to a median OH^+ column density of $N(OH^+) = (1.0 \pm 0.6) \times 10^{15}$ cm^{-2}, or a median hydrogen column density of $N(H) = (6.3 \pm 3.8) \times 10^{22}$ cm^{-2} (see Table 3 for the underlying

[12] In principle, heating from hard radiation sources such as X-rays cannot be ruled out based on the current data alone, even if it is not our preferred explanation due to the lack of other evidence for the presence of hard X-ray sources in these galaxies.

Table 4

Herschel/SPIRE and 870 μm fluxes, CO($J = 9\rightarrow8$) Luminosities, and Parameters Obtained from Dust Spectral Energy Distribution Fitting to Our Sample and Four Sources in the Literature (Including Two Secondary Sources from the Master Sample)

Name	Redshift	S_{250} (mJy)	S_{350} (mJy)	S_{500} (mJy)	S_{870}[a] (mJy)	$T_{\rm dust}$ (K)	$\beta_{\rm IR}$	$\lambda_{\rm peak}$ (μm)	λ_0 (μm)	$L_{\rm FIR}$[b,c] ($10^{12}\,L_\odot$)	$L_{\rm IR}$[b,c,d] ($10^{12}\,L_\odot$)	$L'_{\rm CO(9-8)}$[b,e] ($10^{10}\,L_l$)	$L_{\rm CO(9-8)}$[b] ($10^{8}\,L_\odot$)	References
HeLMS-5	2.2919	312 ± 6	244 ± 7	168 ± 8	49 ± 5	$66.5^{+5.1}_{-6.8}$	$2.05^{+0.48}_{-0.45}$	74^{+4}_{-3}	205^{+22}_{-52}	$40.0^{+1.4}_{-1.6}$	$68.1^{+6.7}_{-5.7}$	2.92 ± 0.45	10.4 ± 1.6	1
HXMM-01	2.3079	180 ± 7	192 ± 8	132 ± 7	29 ± 3	$57.8^{+1.4}_{-2.8}$	$2.52^{+0.18}_{-0.11}$	88^{+4}_{-2}	236^{+11}_{-37}	$22.8^{+1.0}_{-0.4}$	$37.3^{+1.8}_{-1.5}$	2.37 ± 0.39	8.5 ± 1.4	1
HeLMS-9	2.3934	166 ± 6	195 ± 6	135 ± 7		$43.0^{+7.3}_{-8.6}$	$1.82^{+0.23}_{-0.23}$	95^{+3}_{-2}	138^{+58}_{-89}	$21.2^{+1.5}_{-1.6}$	$33.4^{+1.1}_{-7.0}$	2.32 ± 0.45	8.3 ± 1.6	1
HeLMS-61	2.4022	148 ± 6	187 ± 6	147 ± 9		$42.7^{+5.4}_{-7.3}$	$1.91^{+0.32}_{-0.31}$	101^{+4}_{-3}	170^{+51}_{-87}	$19.3^{+1.3}_{-1.4}$	$30.3^{+0.7}_{-5.7}$	1.33 ± 0.17	4.73 ± 0.60	1
HeLMS-45	2.4726	214 ± 7	218 ± 7	172 ± 9		$58.0^{+2.7}_{-3.6}$	$2.70^{+0.38}_{-0.35}$	87^{+4}_{-3}	208^{+8}_{-24}	$31.2^{+1.3}_{-1.5}$	$46.3^{+2.8}_{-4.5}$	6.92 ± 0.99	24.7 ± 3.5	1
J0210+0016	2.5534	826 ± 7	912 ± 7	717 ± 8	167 ± 4	$59.8^{+6.3}_{-8.6}$	$2.01^{+0.07}_{-0.14}$	87^{+5}_{-3}	256^{+63}_{-80}	$130.6^{+3.4}_{-6.8}$	$262.0^{+70.0}_{-91.5}$	7.43 ± 0.66	26.5 ± 2.4	1
HeLMS-44	2.6895	271 ± 6	336 ± 6	263 ± 8		$50.3^{+2.2}_{-4.2}$	$2.15^{+0.28}_{-0.26}$	93^{+3}_{-1}	197^{+3}_{-51}	$47.7^{+1.5}_{-2.0}$	$73.7^{+0.2}_{-11.6}$	4.86 ± 0.80	17.3 ± 2.9	1
Orochi	3.3903	92 ± 7	122 ± 8	113 ± 7	63 ± 6	$55.0^{+1.3}_{-1.5}$	$2.75^{+0.26}_{-0.27}$	93^{+3}_{-2}	274^{+11}_{-16}	$27.4^{+1.0}_{-0.8}$	$48.7^{+1.3}_{-1.1}$	2.50 ± 0.38	8.9 ± 1.4	1
HeLMS-59	3.4346	193 ± 7	252 ± 6	202 ± 8		$53.7^{+6.6}_{-9.4}$	$1.69^{+0.18}_{-0.20}$	79^{+2}_{-1}	127^{+50}_{-77}	$60.1^{+1.6}_{-1.6}$	$92.5^{+5.0}_{-14.2}$	5.65 ± 0.63	20.1 ± 2.3	1
HeLMS-62	3.5027	151 ± 6	209 ± 6	205 ± 8		$56.1^{+2.0}_{-2.1}$	$2.21^{+0.44}_{-0.43}$	88^{+3}_{-2}	209^{+22}_{-26}	$52.1^{+1.2}_{-1.2}$	$76.8^{+2.1}_{-4.8}$	7.7 ± 1.5	27.6 ± 5.4	1
HeLMS-65	3.7966	36 ± 7	49 ± 6	72 ± 7	23 ± 4	$53.6^{+7.7}_{-7.9}$	$2.10^{+0.21}_{-0.21}$	90^{+7}_{-7}	205^{+50}_{-51}	$15.7^{+1.4}_{-1.4}$	$24.2^{+3.1}_{-4.1}$	1.20 ± 0.28	4.3 ± 1.0	1
HeLMS-28	4.1625	113 ± 7	177 ± 6	209 ± 8	82 ± 4	$53.8^{+5.0}_{-6.8}$	$1.74^{+0.16}_{-0.17}$	82^{+2}_{-2}	150^{+24}_{-48}	$63.5^{+1.7}_{-1.6}$	$97.3^{+18.5}_{-12.2}$	7.21 ± 0.60	25.7 ± 2.2	1
HeLMS-10	4.3726	88 ± 6	129 ± 6	155 ± 7	82 ± 5	$58.8^{+3.8}_{-3.2}$	$1.66^{+0.32}_{-0.33}$	82^{+3}_{-3}	208^{+40}_{-39}	$53.7^{+1.6}_{-1.6}$	$88.0^{+14.8}_{-12.0}$	4.39 ± 0.78	15.7 ± 2.8	1
HXMM-30	5.094	30 ± 5	50 ± 8	55 ± 7	28 ± 2	$74.2^{+4.7}_{-4.6}$	$2.64^{+0.37}_{-0.39}$	69^{+4}_{-4}	242^{+29}_{-34}	$24.7^{+1.8}_{-1.7}$	$44.1^{+4.2}_{-6.4}$	2.56 ± 0.52	9.2 ± 1.9	1
HeLMS-34	5.1614	62 ± 6	104 ± 6	116 ± 7	41 ± 3	$63.0^{+7.8}_{-8.3}$	$1.36^{+0.14}_{-0.18}$	66^{+2}_{-2}	93^{+50}_{-64}	$53.8^{+2.1}_{-2.0}$	$86.5^{+5.1}_{-7.8}$	6.98 ± 0.67	24.9 ± 2.4	1
HLock-102	5.2915	56 ± 4	118 ± 4	139 ± 4	70 ± 7	$55.7^{+5.1}_{-7.5}$	$1.80^{+0.07}_{-0.08}$	73^{+2}_{-1}	99^{+31}_{-43}	$68.2^{+1.5}_{-1.3}$	$96.7^{+3.4}_{-5.0}$	12.1 ± 1.9	43.1 ± 6.7	1
ADFS-27	5.6550	14 ± 2	19 ± 2	24 ± 2	25 ± 2	$59.2^{+3.3}_{-4.1}$	$2.52^{+0.19}_{-0.17}$	85^{+5}_{-4}	191^{+11}_{-19}	$15.8^{+1.0}_{-1.9}$	$23.8^{+2.3}_{-2.2}$	2.48 ± 0.06	8.84 ± 0.20	2, 3
HFLS3	6.3369	12 ± 2	32 ± 2	47 ± 3	33 ± 2	$63.3^{+5.4}_{-5.8}$	$1.94^{+0.07}_{-0.09}$	73^{+2}_{-1}	142^{+25}_{-27}	$29.3^{+1.4}_{-1.3}$	$55.0^{+3.0}_{-2.2}$	4.51 ± 0.73	16.1 ± 2.6	4, 5
Literature:														
SDP-17b[f]	2.3051	354 ± 7	339 ± 8	220 ± 9	55 ± 3	$60.3^{+2.8}_{-4.8}$	$2.32^{+0.25}_{-0.24}$	83^{+4}_{-3}	204^{+13}_{-27}	$45.3^{+1.7}_{-2.2}$	$70.9^{+3.6}_{-9.5}$			6
Eyelash	2.3259	366 ± 55	429 ± 64	325 ± 49	106 ± 12	$48.3^{+1.1}_{-2.0}$	$2.81^{+0.18}_{-0.17}$	105^{+3}_{-2}	223^{+10}_{-25}	$44.9^{+2.9}_{-1.9}$	$66.2^{+4.1}_{-2.8}$	1.19 ± 0.56	4.2 ± 2.0	7, 8
HerBS-89a	2.9497	72 ± 6	103 ± 6	96 ± 7	53 ± 4	$49.7^{+2.6}_{-2.8}$	$2.27^{+0.10}_{-0.10}$	102^{+5}_{-5}	256^{+20}_{-22}	$16.8^{+1.0}_{-1.0}$	$26.0^{+0.7}_{-3.1}$	0.88 ± 0.10	3.14 ± 0.37	9
HLock-01[f]	2.9574	425 ± 10	340 ± 10	233 ± 11	53 ± 1	$77.4^{+2.0}_{-3.0}$	$1.93^{+0.17}_{-0.19}$	64^{+1}_{-1}	151^{+15}_{-20}	$87.1^{+1.9}_{-1.1}$	$176.7^{+4.7}_{-2.8}$	6.3 ± 1.6	22.5 ± 5.8	10, 11, 12

Notes. [1] this work; [2–5] Riechers et al. (2013, 2017, 2020b, 2021); [6] Bussmann et al. (2013); [7] Swinbank et al. (2010); [8] Danielson et al. (2011); [9] Berta et al. (2021); [10] Conley et al. (2011); [11] Riechers et al. (2011); [12] Scott et al. (2011).

[a] Fluxes for J0210+0016, HeLMS-28, 10, HLock-102, and HerBS-89a are measured at 850 μm. Fluxes for HeLMS-5, HFLS3, SDP-17b, the Eyelash, and HLock-01 are measured at 880 μm.

[b] Apparent values not corrected for gravitational magnification where applicable. Published lens magnification factors are HeLMS-5 $\mu_{\rm L} = 8.3 \pm 0.6$ (Dye et al. 2018); HXMM-01 subcomponents: $\mu_{\rm L} = 1.39 \pm 0.19$; 1.21 ± 0.01; 1.29 ± 0.15 (Bussmann et al. 2015); J0210+0016 $\mu_{\rm L} = 14.7 \pm 0.3$ (Geach et al. 2018); Orochi $\mu_{\rm L} = 5.33 \pm 0.19$ (Bussmann et al. 2015); HLock-102 $\mu_{\rm L} = 12.5 \pm 1.2$ (Riechers et al. 2020b); HFLS3 $\mu_{\rm L} = 1.8 \pm 0.6$ (Riechers et al. 2020b); SDP17b $\mu_{\rm L} = 4.9 \pm 0.7$ (Bussmann et al. 2013); Eyelash $\mu_{\rm L} = 37.5 \pm 4.5$ (Swinbank et al. 2011); HerBS-89a $\mu_{\rm L} = 5.05 \pm 0.03$ (Berta et al. 2021); HLock-01 $\mu_{\rm L} = 10.9 \pm 0.7$ (Gavazzi et al. 2011).

[c] $L_{\rm FIR}$ ($L_{\rm IR}$) is integrated over the 42.5–122.5 μm (8–1000 μm) range in the rest frame.

[d] Multiply $L_{\rm IR}$ by a factor of 1.0×10^{-10} to obtain apparent star formation rates (SFRs), under the assumption of a Chabrier (2003) stellar initial mass function.

[e] Given in units of $L_l = {\rm K\ km\ s^{-1}\ pc^2}$.

[f] Source is also part of the GADOT master sample, but not reanalyzed with the same methods as used for the sample studied here.

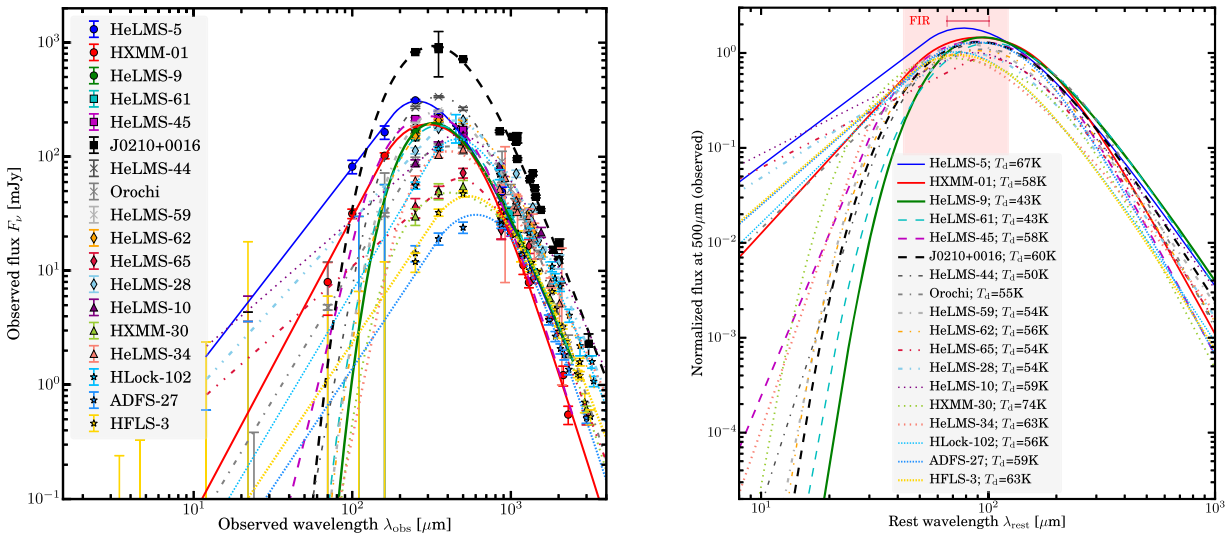

Figure 10. Spectral energy distributions of the GADOT sample and MBB SED fits in the observed frame (left; data points and lines), and models in the rest frame, normalized to the observed 500 μm flux (right), including ADFS-27 and HFLS3 (Riechers et al. 2013, 2017, 2021). The shaded region indicates the wavelength range used to calculate the far-infrared luminosities, while the entire range shown is used to calculate total infrared luminosities. The bar at the top indicates the range in peak wavelengths.

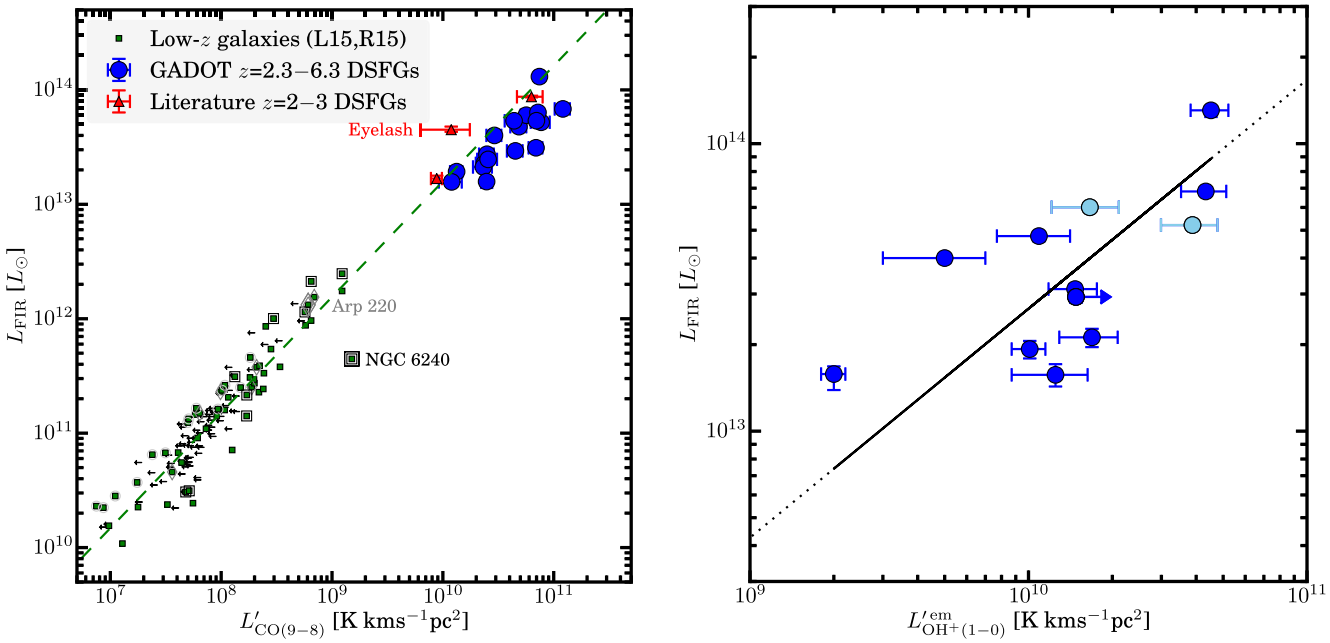

Figure 11. Left: CO(J = 9→8)–FIR luminosity relation for the GADOT sample (blue dots), other Herschel-selected DSFGs, and the Cosmic Eyelash (red triangles; see Table 4) and nearby galaxies (green symbols and upper limit arrows; Liu et al. 2015; L15). The dashed line is the fit to the nearby galaxy sample proposed by Liu et al. (2015), which has a power-law slope of $N = 1.01$. Fluxes were not corrected for gravitational lensing magnification. Given the linear slope of the relation, lensing effects are unimportant unless the dust and warm molecular gas are differentially lensed relative to each other. Gray circle, diamond, and square outlines indicate Class I, II, and III sources from the HerCULES survey as identified by Rosenberg et al. (2015; R15), respectively. Higher classes indicate higher CO excitation. The GADOT sample lies between the luminosity ratios of Arp 220 and NGC 6240. The systematic offset of the sample toward higher $L'_{CO(9-8)}$ may indicate a more important role of shock heating compared to the nearby star-forming galaxies. Right: OH^+ emission—FIR luminosity relation (solid line) for the GADOT sample. Light blue dots indicate the sources for which $OH^+(1_2 \rightarrow 0_1)$ is used instead of $OH^+(1_1 \rightarrow 0_1)$ because the emission components in the latter were not fully covered.

assumptions). For a typical DSFG diameter of 2 kpc (e.g., ADFS-27; Riechers et al. 2021), this corresponds to a neutral hydrogen mass of $M(H) \sim 2 \times 10^9\,M_\odot$.

We then compare the results to SED-based physical quantities that are, to first order, independent of lensing magnification. In the top row of Figure 12, T_{dust}, λ_0, and λ_{peak} are shown as a function of redshift. There are no clear trends except for a potential weak increase in T_{dust} toward higher redshift, and a corresponding weak blueshifting of λ_{peak}. This weak trend is likely primarily due to the underlying selection function of Herschel at 250–500 μm and is thus consistent with no strong underlying redshift evolution within the uncertainties.

The remaining panels show the same quantities in relation to the peak and integral optical depths. There is no detectable trend with λ_0, such that we do not find evidence for increased OH^+ absorption in systems that have higher dust opacity near the wavelengths of the OH^+ lines. This is perhaps expected because the OH^+ absorption is caused by gas in front of the

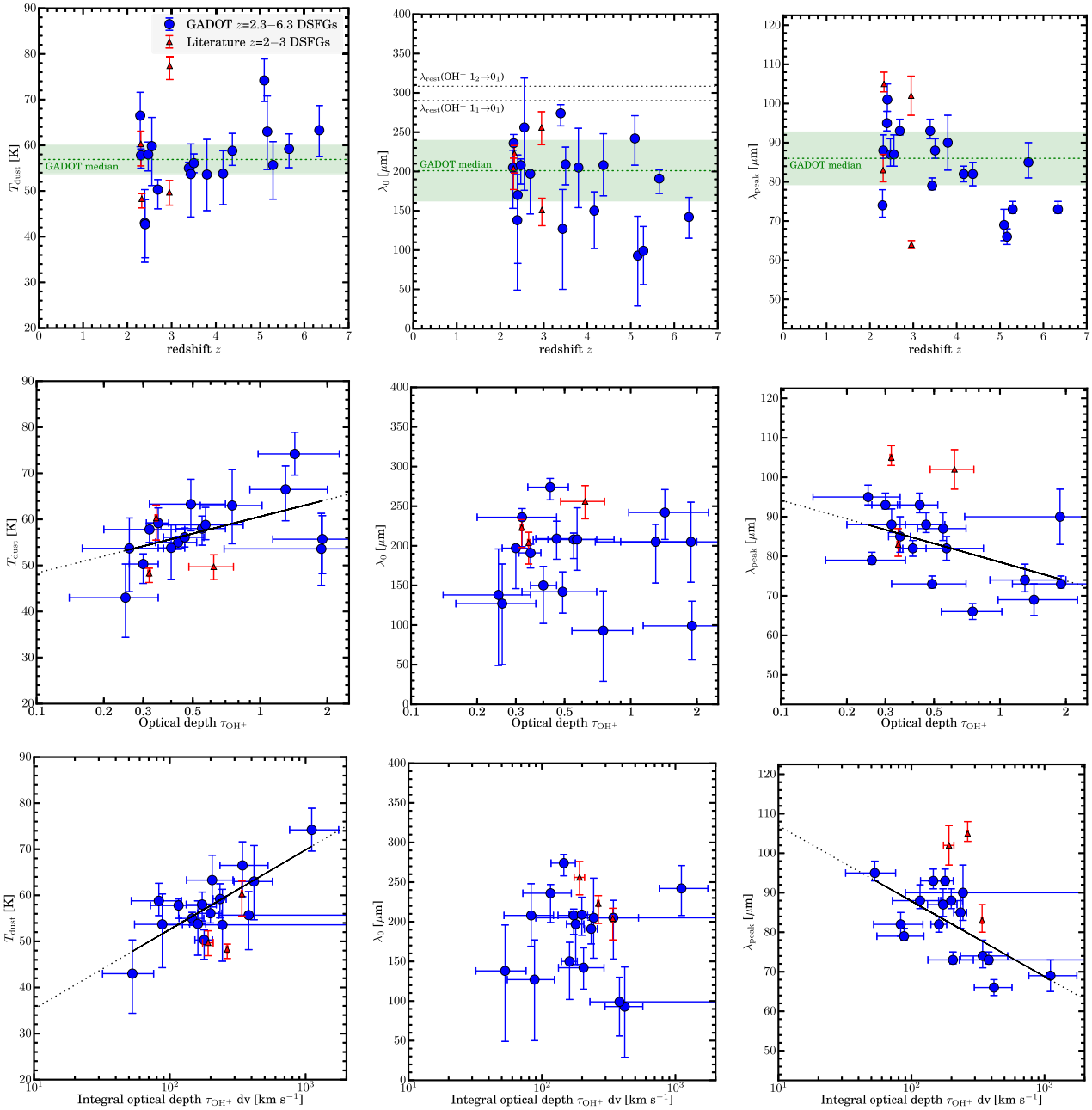

Figure 12. Relations between the dust temperature, the wavelength at which the optical depth reaches unit, and the SED peak wavelength (left to right) as a function of wavelength, OH^+ optical depth, and OH^+ integral optical depth (top to bottom) for the GADOT sample (blue dots) and three $z = 2$–3 DSFGs from the literature (red triangles; see Table 4). For reference, the median values and median absolute deviation of the GADOT sample are shown in the top panels as the dotted green lines and shaded region, and the rest wavelengths of the OH^+ transitions in this study are indicated in the top middle panel (showing that the dust optical depth is below unity for the sample at the OH^+ wavelengths). There appears to be a correlation (black lines; see Table 5 for the fit parameters) between the OH^+ integral optical depth and the dust temperature (and an inverse correlation with the SED peak wavelength), and a similar but weaker correlation between the OH^+ optical depth and the dust temperature (and inversely, with peak wavelength).

dust continuum. On the other hand, there appears to be a significant trend of increased OH^+ absorption depth toward higher dust temperatures (or correspondingly, toward shorter wavelengths of the SED peak). The trend appears to be tighter for the integral optical depth (see Table 5).

There are two potential factors that may explain such a trend. First, the OH^+ $2 \rightarrow 1$ lines (which reduce the upper level populations of the $1_1 \rightarrow 0_1$ and $1_2 \rightarrow 0_1$ transitions if seen in absorption) lie at ∼1892–2029 GHz, or 148–158 μm, i.e., close

Table 5
Best-fit Dust Opacity Correlations with a Functional Form $y = a + \log(b \cdot x/[\text{unit x}])[\text{unit y}]$

Parameters	a	b
τ_{OH+}, T_{dust}	60.6 ± 2.0 K	5.3 ± 2.4
$\tau_{OH+}dv$, T_{dust}	18.1 ± 8.8 K	7.5 ± 1.6
τ_{OH+}, λ_{peak}	79 ± 3 μm	-6.8 ± 3.1
$\tau_{OH+}dv$, λ_{peak}	126 ± 13 μm	-8.3 ± 2.5

to or shortward of λ_0 for most of the GADOT sample. These transitions are observed in absorption in the archetypal ultraluminous infrared galaxy (ULIRG) Arp 220 (González-Alfonso et al. 2013), and tentatively, in the $z = 6.34$ starburst HFLS3 (based on the data shown by Riechers et al. 2013). As such, it is conceivable that the observed trend could be due to the increased availability of 148–158 μm photons as the SED peak shifts toward shorter wavelengths, which results in an increased pumping efficiency out of the upper level of the $1_1 \rightarrow 0_1$ and $1_2 \rightarrow 0_1$ transitions.

Second, the sources with higher $T_{\rm dust}$ may simply be warmer because they are more compact, such that they have higher $\Sigma_{\rm FIR}$ and $\Sigma_{\rm SFR}$ surface densities. Smaller sizes then lead to a higher density of supernovae once the most massive stars end their life cycles. Because the supernova rate is proportional to the rate of cosmic-ray production, this would result in an increased cosmic-ray energy density. The central regions of the high $T_{\rm dust}$ DSFGs in the GADOT sample thus may resemble giant cosmic-ray-dominated regions, rather than ensembles of photon-dominated regions, i.e., similar to what has been discussed for ULIRG nuclei (e.g., Papadopoulos Papadopoulos 2010; González-Alfonso et al. 2013). Because cosmic rays are likely the main production mechanism for molecular ions such as OH^+, the increased cosmic-ray energy density would then result in an increased abundance of OH^+ for higher $T_{\rm dust}$ sources, causing stronger OH^+ absorption and therefore higher OH^+ optical depth. High cosmic-ray energy densities could also explain the comparatively high CO excitation in this sample, as a possible alternative to the shock-induced CO excitation scenario.

In principle, the OH^+ abundance can also be increased in environments exposed to radiation fields associated with X-ray dominated regions (XDRs) around AGN (see also the discussion by González-Alfonso et al. 2013). At the same time, AGN can increase the dust temperature as an additional heating source. A contribution like this can certainly be relevant for local enhancements near an AGN. However, given the high optical depth of the dust, it is unlikely that the radiation from AGN can penetrate to large radii even if buried AGN are present in our sample, such that it remains unclear that the OH^+ production could be sufficiently increased on large enough scales to fully explain the observed trend.

5. Conclusions

We have detected 18 CO($J = 9 \rightarrow 8$) emission lines and 23 ground-state OH^+ absorption, emission, and P-Cygni-shaped lines toward a sample of 18 Herschel-selected massive DSFGs at $z = 2.3$–6.3 as part of the GADOT Galaxy Survey (including two previously published targets). CO($J = 9 \rightarrow 8$) emission from warm, dense molecular gas is detected in all targets, at higher line luminosities than expected from the $L'_{\rm CO(9-8)}$–$L_{\rm FIR}$ relation for nearby star-forming galaxies. This may suggest that shock excitation of the molecular gas impacted by galactic winds is more prevalent in DSFGs in the early universe than in the bulk of nearby star-forming galaxies, but similar to what is seen in some of the most active nearby starbursts. The presence of copious amounts of shock-heated, dense gas is also consistent with the strength of the OH^+ emission in the two-thirds of the sample in which it is detected, but high cosmic-ray energy densities would provide a possible alternative explanation for the observed trends. One of the galaxies is thought to contain an AGN and shows a spatial offset between the $OH^+$and dust emission peaks. This may indicate a local enhancement of OH^+ due to the AGN radiation field, but an AGN contribution is not strictly required to explain its OH^+ properties.

OH^+ absorption is seen in all but two galaxies in the sample, showing that it is ubiquitous among high-z starburst galaxies. This finding on its own appears to imply that the absorbing OH^+ gas is widespread and is not confined to small opening angles, as expected if it resides in an extended gaseous halo. We find a balance between red- and blueshifted OH^+ absorption/emission components in those galaxies that show significant velocity shifts relative to CO, which may suggest that both outflows (as indicated by blueshifted absorption and/or redshifted emission) and inflows (as indicated by the opposite) are prevalent. Some of the systems showing evidence for outflows have outflow velocities that likely exceed the escape velocities of the galaxies. As such, star formation feedback appears to be important in the evolution of massive galaxies in their most active phase, but higher spatial resolution observations are required to study the gas kinematics and balance of outflows versus inflows on scales that come closer to resolving the starburst nuclei for the bulk of the sample and to better separate systemic gas components from gas flows.

We find a correlation between the OH^+ absorption optical depth and the dust temperature, and an inverse correlation of the former with the peak wavelength of the dust SED. We suggest that this is due to the fact that higher $T_{\rm dust}$ DSFGs typically are more compact, showing higher $\Sigma_{\rm FIR}$ and $\Sigma_{\rm SFR}$. This yields an increased cosmic-ray energy density through a high density of supernovae, and thus an increased production of OH^+ ions—hence stronger OH^+ absorption. In principle, this effect could also contribute to the high CO excitation of the sample. Another contributing effect may be the enhanced availability of $\sim$150 μm photons for higher $T_{\rm dust}$ DSFGs, which could lead to an enhanced pumping efficiency out of the upper levels of the observed OH^+ transitions.

Our findings provide an improved understanding of the role of gas flows in the evolution of massive star-forming galaxies in the early universe. This places the initial studies of high-J CO and OH^+ lines in distant galaxies on a firmer statistical footing. Detailed studies show that when they are associated with outflows, these gas flows can expel gas from the star-forming regions at high rates, regulating the growth of these already massive systems (e.g., Riechers et al. 2021). While inflows were previously thought to be rare (e.g., Berta et al. 2021), our current observations may suggest (within a factor of $\sim$1–2.5) a similar prevalence of OH^+ outflows versus inflows, and that it is relatively common to see OH^+ emission components along with the absorption. If confirmed, this may suggest that the gas inflows are not confined to small opening angles. On the other hand, the detectability of emission components from the gas flows in a largely (>80%) strongly gravitationally lensed galaxy sample with typical magnification factors of $\sim$5–40 make it likely that the typical sizes of the entire systems are perhaps only a few kiloparsecs at most, given the small regions with high amplification factors in most lensing configurations. This is consistent with the observed sizes of the continuum emission where magnification factors are known. The high detection rate suggests that OH^+ nondetections, as seen in the southern component of the (not strongly lensed) $z = 5.66$ merger ADFS-27 (Riechers et al. 2021), are relatively rare among DSFGs, and/or that high spatial resolution observations are required to identify the galaxy or merger components associated with the OH^+ absorption or emission. It also may suggest that processes

on scales of a few kiloparsec are key to explain the origin of the OH^+ absorption/emission in complex merging systems such as ADFS-27, or similar lower-redshift systems such as HXMM-01.

Observations in the short millimeter to submillimeter wavelength regime with ALMA and NOEMA are critical to give access to a broad range in line diagnostics in the early universe that Herschel has established in the nearby universe based on samples of tens of galaxies. This study, which was carried out as part of the GADOT Galaxy Survey, provides the first investigation of a sizeable sample of high-redshift galaxies in the OH^+ diagnostic lines, which confirms that OH^+ is a prime tracer of the physical properties and chemical composition of the ISM throughout cosmic history, and the perhaps most easily accessible tracer of molecular outflows and inflows. Future work on the GADOT sample, together with complementary investigations (e.g., K. Butler et al. 2021, in preparation), will expand the standard toolkit for these studies to additional molecular species, and will provide a more comprehensive study of the CO line ladders. Because the properties of the ISM set the initial conditions for star formation, such comprehensive studies are critical to fully understand the galaxy formation process, and in which ways it may differ at the high-mass, high-luminosity end.

We thank the anonymous referee for helpful suggestions that led to some valuable clarifications in this work. The authors thank Daizhong Liu for sharing the local galaxy source data displayed in the CO($J = 9 \rightarrow 8$)—FIR relation figure. D.R. acknowledges support from the National Science Foundation under grant numbers AST-1614213 and AST-1910107. D.R. also acknowledges support from the Alexander von Humboldt Foundation through a Humboldt Research Fellowship for Experienced Researchers. A.C. acknowledges support from NASA grant 80NSSC20K0437. The National Radio Astronomy Observatory is a facility of the National Science Foundation operated under cooperative agreement by Associated Universities, Inc. This paper makes use of the following ALMA data: ADS/JAO. ALMA# 2016.2.00105.S; 2018.1.00922.S; 2017.1.00235.S; and 2018.1.00966.S. ALMA is a partnership of ESO (representing its member states), NSF (USA) and NINS (Japan), together with NRC (Canada) and NSC and ASIAA (Taiwan), in cooperation with the Republic of Chile.

Facilities: ALMA, ATCA, Hubble (ACS and WFC3).

Software: CASA package (v5.6.1; McMullin et al. 2007).

ORCID iDs

Dominik A. Riechers https://orcid.org/0000-0001-9585-1462
Asantha Cooray https://orcid.org/0000-0002-3892-0190
Ismael Pérez-Fournon https://orcid.org/0000-0002-2807-6459
Roberto Neri https://orcid.org/0000-0002-7176-4046

References

Amvrosiadis, A., Eales, S. A., Negrello, M., et al. 2018, MNRAS, 475, 4939
Asboth, V., Conley, A., Sayers, J., et al. 2016, MNRAS, 462, 1989
Benz, A. O., Bruderer, S., van Dishoeck, E. F., et al. 2010, A&A, 521, L35
Berta, S., Young, A. J., Cox, P., et al. 2021, A&A, 646, A122
Bialy, S., Neufeld, D., Wolfire, M., Sternberg, A., & Burkhart, B. 2019, ApJ, 885, 109
Bradford, C. M., Aguirre, J. E., Aikin, R., et al. 2009, ApJ, 705, 112
Brown, R. L., & Vanden Bout, P. A. 1991, AJ, 102, 1956
Bussmann, R. S., Pérez-Fournon, I., Amber, S., et al. 2013, ApJ, 779, 25
Bussmann, R. S., Riechers, D., Fialkov, A., et al. 2015, ApJ, 812, 43
Carilli, C. L., & Walter, F. 2013, ARA&A, 51, 105
Chabrier, G. 2003, PASP, 115, 763
Conley, A., Cooray, A., Vieira, J. D., et al. 2011, ApJL, 732, L35
Danielson, A. L. R., Swinbank, A. M., Smail, I., et al. 2011, MNRAS, 410, 1687
Decarli, R., Aravena, M., Boogaard, L., et al. 2020, ApJ, 902, 110
Dowell, C. D., Conley, A., Glenn, J., et al. 2014, ApJ, 780, 75
Downes, D., Neri, R., Wiklind, T., Wilner, D. J., & Shaver, P. A. 1999, ApJL, 513, L1
Dye, S., Furlanetto, C., Dunne, L., et al. 2018, MNRAS, 476, 4383
Eales, S., Dunne, L., Clements, D., et al. 2010, PASP, 122, 499
Falgarone, E., Zwaan, M. A., Godard, B., et al. 2017, Natur, 548, 430
Fu, H., Cooray, A., Feruglio, C., et al. 2013, Natur, 498, 338
García-Burillo, S., Graciá-Carpio, J., Guélin, M., et al. 2006, ApJL, 645, L17
Gavazzi, R., Cooray, A., Conley, A., et al. 2011, ApJ, 738, 125
Geach, J. E., Ivison, R. J., Dye, S., & Oteo, I. 2018, ApJL, 866, L12
Geach, J. E., More, A., Verma, A., et al. 2015, MNRAS, 452, 502
Gerin, M., de Luca, M., Black, J., et al. 2010, A&A, 518, L110
Gómez-Guijarro, C., Riechers, D. A., Pavesi, R., et al. 2019, ApJ, 872, 117
González-Alfonso, E., Fischer, J., Bruderer, S., et al. 2013, A&A, 550, A25
Greenslade, J., Clements, D. L., Petitpas, G., et al. 2020, MNRAS, 496, 2315
Harrington, K. C., Yun, M. S., Cybulski, R., et al. 2016, MNRAS, 458, 4383
Hodge, J. A., & da Cunha, E. 2020, RSOS, 7, 200556
Hollenbach, D., Kaufman, M. J., Neufeld, D., Wolfire, M., & Goicoechea, J. R. 2012, ApJ, 754, 105
Ikarashi, S., Kohno, K., Aguirre, J. E., et al. 2011, MNRAS, 415, 3081
Indriolo, N., Bergin, E. A., Falgarone, E., et al. 2018, ApJ, 865, 127
Indriolo, N., Neufeld, D. A., Gerin, M., et al. 2015, ApJ, 800, 40
Kamenetzky, J., Rangwala, N., Glenn, J., Maloney, P. R., & Conley, A. 2014, ApJ, 795, 174
Kamenetzky, J., Glenn, J., Rangwala, N., et al. 2012, ApJ, 753, 70
Klitsch, A., Péroux, C., Zwaan, M. A., et al. 2019, MNRAS, 490, 1220
Lenkić, L., Bolatto, A. D., Förster Schreiber, N. M., et al. 2020, AJ, 159, 190
Li, J., Wang, R., Riechers, D., et al. 2020, ApJ, 889, 162
Liu, D., Gao, Y., Isaak, K., et al. 2015, ApJL, 810, L14
McMullin, J. P., Waters, B., Schiebel, D., Young, W., & Golap, K. 2007, in ASP Conf. Ser., 376, Astronomical Data Analysis Software and Systems XVI, ed. R. A. Shaw, F. Hill, & D. J. Bell (San Francisco, CA: ASP), 127
Meijerink, R., Kristensen, L. E., Weiß, A., et al. 2013, ApJL, 762, L16
Nayyeri, H., Keele, M., Cooray, A., et al. 2016, ApJ, 823, 17
Neufeld, D. A., Goicoechea, J. R., Sonnentrucker, P., et al. 2010, A&A, 521, L10
Oliver, S. J., Bock, J., Altieri, B., et al. 2012, MNRAS, 424, 1614
Oteo, I., Ivison, R. J., Negrello, M., et al. 2017, arXiv:1709.04191
Papadopoulos, P. P. 2010, ApJ, 720, 226
Planck Collaboration, Abergel, A., Ade, P. A. R., et al. 2011, A&A, 536, A25
Rangwala, N., Maloney, P. R., Glenn, J., et al. 2011, ApJ, 743, 94
Riechers, D. A., Walter, F., Carilli, C. L., et al. 2006, ApJL, 645, L13
Riechers, D. A., Weiß, A., Walter, F., & Wagg, J. 2010, ApJ, 725, 1032
Riechers, D. A., Cooray, A., Omont, A., et al. 2011, ApJL, 733, L12
Riechers, D. A., Bradford, C. M., Clements, D. L., et al. 2013, Natur, 496, 329
Riechers, D. A., Leung, T. K. D., Ivison, R. J., et al. 2017, ApJ, 850, 1
Riechers, D. A., Pavesi, R., Sharon, C. E., et al. 2019, ApJ, 872, 7
Riechers, D. A., Boogaard, L. A., Decarli, R., et al. 2020a, ApJL, 896, L21
Riechers, D. A., Nayyeri, H., Burgarella, D., et al. 2021, ApJ, 907, 62
Riechers, D. A., Hodge, J. A., Pavesi, R., et al. 2020b, ApJ, 895, 81
Rosenberg, M. J. F., van der Werf, P. P., Aalto, S., et al. 2015, ApJ, 801, 72
Scott, K. S., Lupu, R. E., Aguirre, J. E., et al. 2011, ApJ, 733, 29
Solomon, P. M., Radford, S. J. E., & Downes, D. 1992, Natur, 356, 318
Spinoglio, L., Pereira-Santaella, M., Busquet, G., et al. 2012, ApJ, 758, 108
Stanley, F., Knudsen, K. K., Aalto, S., et al. 2021, A&A, 646, A178
Su, T., Marriage, T. A., Asboth, V., et al. 2017, MNRAS, 464, 968
Swinbank, A. M., Smail, I., Longmore, S., et al. 2010, Natur, 464, 733
Swinbank, A. M., Papadopoulos, P. P., Cox, P., et al. 2011, ApJ, 742, 11
van der Tak, F. F. S., Nagy, Z., Ossenkopf, V., et al. 2013, A&A, 560, A95
van der Werf, P. P., Isaak, K. G., Meijerink, R., et al. 2010, A&A, 518, L42
Walter, F., Decarli, R., Sargent, M., et al. 2014, ApJ, 782, 79
Walter, F., Carilli, C., Neeleman, M., et al. 2020, ApJ, 902, 111
Wardlow, J. L., Cooray, A., De Bernardis, F., et al. 2013, ApJ, 762, 59
Weiß, A., Downes, D., Neri, R., et al. 2007, A&A, 467, 955
Wyrowski, F., Menten, K. M., Güsten, R., & Belloche, A. 2010, A&A, 518, A26
Xue, R., Fu, H., Isbell, J., et al. 2018, ApJL, 864, L11